NATIONAL AND KAPODISTRIAN UNIVERSITY OF ATHENS

MASTER THESIS

Particle Acceleration in the Current Sheet of Puslar Magnetospheres

---

Author:
Petros STEFANOU

Supervisor:
Assoc. Pr. Nektarios VLAHAKIS
Co-Supervisor:
Dr. Ioannis CONTOPOULOS

A thesis submitted in fulfillment of the requirements for the degree of Master in Astrophysics

in the

Department of Physics
Section of Astrophysics, Astronomy and Mechanics

June 12, 2019

NATIONAL AND KAPODISTRIAN UNIVERSITY OF ATHENS

Abstract

Faculty Name
Department of Physics
Section of Astrophysics, Astronomy and Mechanics

Master in Astrophysics

Particle Acceleration in the Current Sheet of Puslar Magnetospheres

by Petros STEFANOU

We investigate the mechanism and the origin of high-energy emission from the pulsar magnetosphere. We consider a simple semi-analytic model, the so-called "Ring of Fire", that satisfies global electric current closure. According to this model, a dissipation zone develops in the magnetosphere at the edge of the closed-line region beyond the light cylinder. Electrons and positrons are accelerated inwards and outwards respectively along relativistic Speiser orbits that are deflected in the azimuthial direction by the pulsar's rotation. After they exit the dissipation zone, the outward moving positrons form the equatorial return current sheet, and the inward moving electrons form the separatrix return current sheet. The particles lose their energy via curvature radiation mostly outside of the dissipation zone, along the current sheets. We present the first results of extensive numerical simulations that routinely integrate the particle's equations of motion in a given electromagnetic field with radiation losses, and calculate particle orbits and the resulting high-energy spectra.

Acknowledgements

I would like to express my sincere gratitude to my main supervisor Dr. Ioannis Contopoulos for his constant encouragement an sharing his expertise with me. His mentoring and guidance, as well as his constructive critique, allowed me to gain the most from this thesis. Most importantly, I am thankful for his willingness to push me to my limits and provide me with opportunities to advance in the field.

I wish to thank my co-supervisor Pr. Nektarios Vlahakis for always having his door open for me. His valuable comments gave perspective to my work and helped me overcome many obstacles. He was always eager to support me in any way possible.

I also wish to acknowledge Pr. Apostolos Mastichiadis for his useful comments and his genuine interest in my work. He was always available and willing to answer my questions and give me advice.

Special thanks go to my fellow students for their eagerness to listen and participate in my concerns. They offered me valuable feedback and insightful discussions for which I am grateful. We were on this journey together and I wish the best to all of them.

Lastly, I want to thank my family for their unconditional love and support. They trusted me to follow my own path and thoughtfully ensured the best possible conditions for me to work and study. Their contribution is invaluable.

Contents

List of Figures

List of Abbreviations

DZ	**D**issipation **Z**one
ECS	**E**quatorial **C**urrent **S**heet
SCS	**S**eparatrix **C**urrent **S**heet
LC	**L**ight **C**ylinder
SED	**S**pectral **E**nergy **D**istribution
FFE	**F**orce **F**ree **E**lectrodynamics
PIC	**P**article **I**n **C**ell
MHD	**M**agneto **H**ydro **D**ynamics
E/M	**E**lectro/**M**agnetic
INS	**I**solated **N**eutron **S**tars
RPP	**R**otation **P**owered **P**ulsars
MSP	**Mi**li **S**econd **P**ulsars **CCO**
Central **C**ompact **O**bjects	
INS	**I**solated **N**eutron **S**tars
RRT	**R**otation **R**adio **T**ransients
EOS	**E**quation **O**f **S**tate

1 Introduction

Pulsars (pulsating radio sources) are rotating magnetised neutron stars. In general the physical conditions that occur around them are unique and extreme. As a result pulsars are ideal celestial laboratories for a variety of disciplines: nuclear and particle physics, condensed-matter physics, general theory of relativity and in particular high energy radiation and relativistic magneto-hydrodynamics, which will be the focus of this thesis.

The astrophysical community has been dealing with the observation and study of pulsars for more than half a century. The progress made in understanding these objects is substantial, but there are many important questions to be answered.

In the following sections of chapter 1 we will give the profile of a pulsar and present the fundamentals and preliminaries. In chapter 2 we will discuss the magnetosphere of pulsars ... In chapter 3 we will present our model for high energy emission and in chapter 4 the numerical setup that we used to simulate it. The results we produced are presented and discussed in chapter 5. Finally in chapter 6 we will summarise and suggest the next steps.

1.1 Theoretical Prediction

Shortly after the discovery of the neutron by Chadwick (Chadwick, 1932) in 1932, two astronomers, Baade & Zwicky (Baade and Zwicky, 1934a; Baade and Zwicky, 1934b), proposed that during Supernova explosions small, extremely dense objects could be created in the centre of the exploding star. They suggested that the enormous pressure occurring in the centre of the explosion would be sufficient to enable an "inverse beta-decay" during which electrons and protons are combined to neutrons and neutrinos. Neutrinos could leave the star to carry away a substantial amount of energy, leaving behind a very dense object consisting mostly of neutrons. They called these objects accordingly "neutron stars".

Five years later, Oppenheimer & Volkov (Oppenheimer and Volkoff, 1939) were the first to calculate the expected size and mass of these newly predicted objects. Based on quantum mechanical arguments they computed that neutron stars should have a diameter of about 20 km while containing 1.4 times the mass of the sun. Given this extremely small size expected for these objects, astronomers therefore considered it to be impossible to ever detect neutron stars and hence to verify the predictions by Baade & Zwicky.

1.2 Discovery

The first pulsar was discovered in 1967 by Jocelyn Bell (Hewish et al., 1968). Bell was then a graduate student at the University of Cambridge conducting her PhD thesis research under the supervision of Antony Hewish. Her group's project was to built and operate a large radio telescope to detect signals coming from the, recently discovered, quasars. Analysing the data she noticed a very fast and incredibly steady pulse coming from a certain direction in the sky. After a thorough examination, all of the known galactic, extra-galactic and human-built radio sources were eliminated as possible emitters of the radio signal. Bell had discovered a new celestial radio source. In a short period of time, she discovered three more similar signals from different directions in the sky, which reinforced the legitimacy of the discovery.

Shortly after the publication of the discovery paper, F. Pacini (Pacini, 1967) and T. Gold (Gold, 1968), in independent works, identified pulsars as rotating magnetised neutron stars, confirming the prediction of Baade & Zwicky.

1.3 Physical Properties

In this section, we will briefly discuss the basic features and properties of pulsars.

1.3.1 Creation

In a main sequence star, an equilibrium between the gravitational forces and the pressure generated by the nuclear fusion in the core is established. As soon as the nuclear fuels deplete, gravity dominates and the star collapses to its centre.

The star's core primarily consists of iron. As the collapse proceeds, the density, pressure and temperature of the core increase. This leads to the disintegration of atomic nuclei to alpha particles and creates the conditions for inverse beta decay to occur, that is, electrons and protons combine and produce neutrons and neutrinos.

$$p^+ + e^- \rightarrow n + \nu_e \tag{1.1}$$

Neutrinos escape and carry away a significant portion of the core's energy. As the collapse continues, the density in the core becomes equal to the nuclear density $\rho \simeq 10^{14}\ g/cm^3$ while all the available energy levels are occupied. Neutrons are fermions and obey the Pauli exclusion principle so at this point they cannot be further compressed. This so called 'degenerate neutron pressure' balances out the gravitational force and stops the collapse of the core[1].

The in-falling outer layers are deflected in the core and bounce back, colliding with the rest in-falling matter. This an overwhelmingly violent event that causes an explosion known as supernova. Such explosions result in the creation of an expanding, bright nebula, in the centre of which lies the leftover of the explosion, the newly formatted neutron star.

1.3.2 Rotation and magnetic field

As stated above, pulsars are rapidly rotating, magnetised neutron stars. Their period of rotation lies typically in the range $P \simeq 10^{-3} - 10^{1}\ s$, so they are really fast rotators. They possess enormous magnetic fields, possibly the strongest known in the universe. The value of the field in the stellar surface is between $B \simeq 10^{8} - 10^{15}\ G$, with a typical value of $10^{12}\ G$. The form of the magnetic field is, in a good approximation, that of a dipole and the magnetic axis has an inclination angle a with respect to the rotation axis. These two characteristics enable pulsars to operate

[1] There are two more possible scenarios except that of the neutron star: a) If the progenitor star is sufficiently small ($M_s \leq 8M_\odot$) the pressure of the degenerate electrons is strong enough to balance gravity before the formation of neutrons and a white dwarf with mass $M_{WD} < 1.4M_\odot$ is created. b) if the progenitor star is large ($M_s \geq 20M_\odot$), not even the pressure of the degenerate neutrons is enough to withhold gravity and the entire core collapses to a singularity, forming a black hole.

as efficient particle accelerators. The particles slowly subtract the stored rotational energy of the star and radiate it away via various emission mechanisms. As a result the pulsar slows down and its period of rotation increases with time. The spin-down rate $\dot{P}$ is measurable and falls within the range of 10^{-22} to $10^{-9} s/s$, with the faster rotating pulsars usually having smaller $\dot{P}$. As a pulsar ages, the rate of rotation will become too slow to power the radio-emission mechanism, and it can no longer be detected.

1.3.3 Size, mass and structure

When a stable condition between gravity and degenerate neutron pressure is reached, the expected radius of the resulting core is very small, $r_* \simeq 10\ km$. This is equivalent to the diameter of a typical city.

The surface temperature of the neutron star, at the time of its creation is about $T \simeq 10^{11} - 10^{12} K$. However the vast number of neutrinos that are generated through the inverse beta decay carry away most of the thermal energy and the surface temperature sits at $T \simeq 10^6 K$ shortly after the creation. Blackbody radiation at this temperature peaks at X-rays and is actually observed by modern day telescopes.

Before we proceed, we can give here a rather crude and qualitative argument for the extreme values of the rotational period and the magnetic field of pulsars: when a star of radius $r \simeq 10^6\ km$ shrinks to a core of radius $r \simeq 10\ km$ its surface decreases by a factor of 10^{10}. Thus, conservation of angular momentum and magnetic flux imply that the magnetic field and the angular velocity must correspondingly increase by a factor of 10^{10}. This skyrockets the values of B and Ω and establishes the unique situation under which a pulsar operates.

Neutron star masses can be well measured from binary systems. Usually the observed masses have a value close to $M = 1.4\ M_\odot$ (see fig. 1.1), the Chandrasekhar mass limit for white dwarfs. This is the limit below which the pressure of degenerate electrons can stop the gravitational collapse before the neutron star is created (see fn. 1). The aforementioned values correspond to an average mass density of $\rho \simeq 10^{14} gr/cm^3$ which is the density of the atomic nucleus. In fact the density in the interior of the neutron star far exceeds this value. The physical properties of matter under these extreme conditions can only be studied on the basis of theoretical models, thus, the maximum and minimum permitted values for the mass of the neutron star are not precisely determined. Given an Equation of State (EOS), a mass-radius relation for the neutron star and a corresponding maximum neutron star mass can be derived. There are several proposed EOSs but little evidence to confirm or exclude them. At the very least, there is an upper limit in the maximum possible mass, imposed by general relativity at $M_{max} = 3.2\ M_\odot$. Currently the neutron star mass is, generally considered to be in the range $1 - 3\ M_\odot$ (Kiziltan et al., 2013).

For similar reasons, the exact internal structure of the neutron star is still unclear. Current theoretical models divide the star in five basic regions (see figure 1.2):

- The atmosphere, a very thin, due to the immense gravitational forces, layer consisting of a variety of lighter elements in a fluid/gas state. This is the region where the thermal component of the pulsar spectrum comes from.

- The outer crust, consisting of a lattice of heavy ions (mainly $^{56}_{26}Fe$) and a sea of electrons running through it. These are the only regions that will concern us in the rest of this thesis, as we will show that charges can be extracted from the surface and fill the pulsar surroundings, forming a magnetosphere.

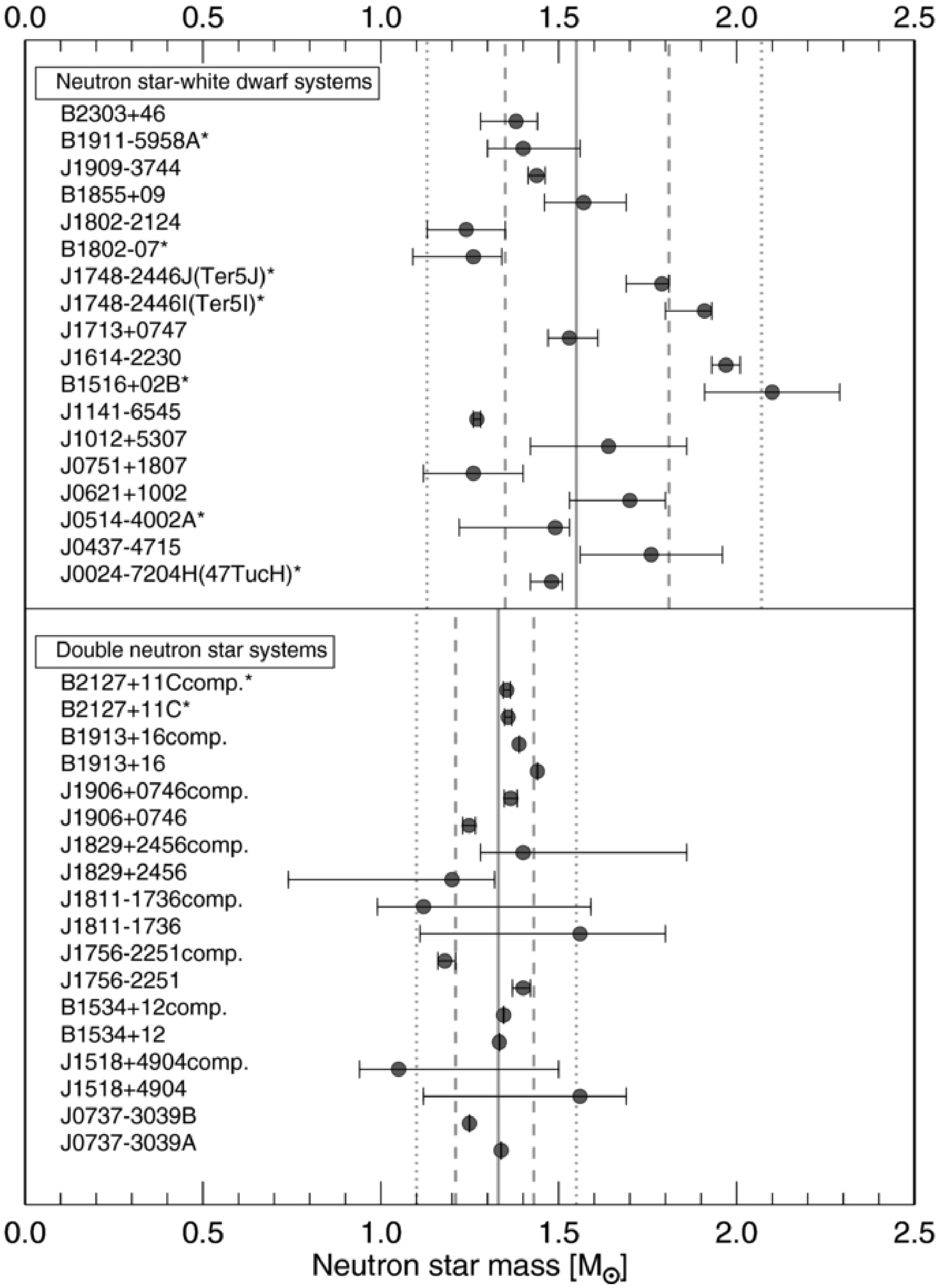

FIGURE 1.1: Measured masses of radio pulsars. All error bars indicate the central 68% confidence limits. Vertical solid lines are the peak values of the underlying mass distribution for DNS (m = 1.33M) and NS–WD (m = 1.55M) systems. Systems marked with asterisks are found in globular clusters (Kiziltan et al., 2013).

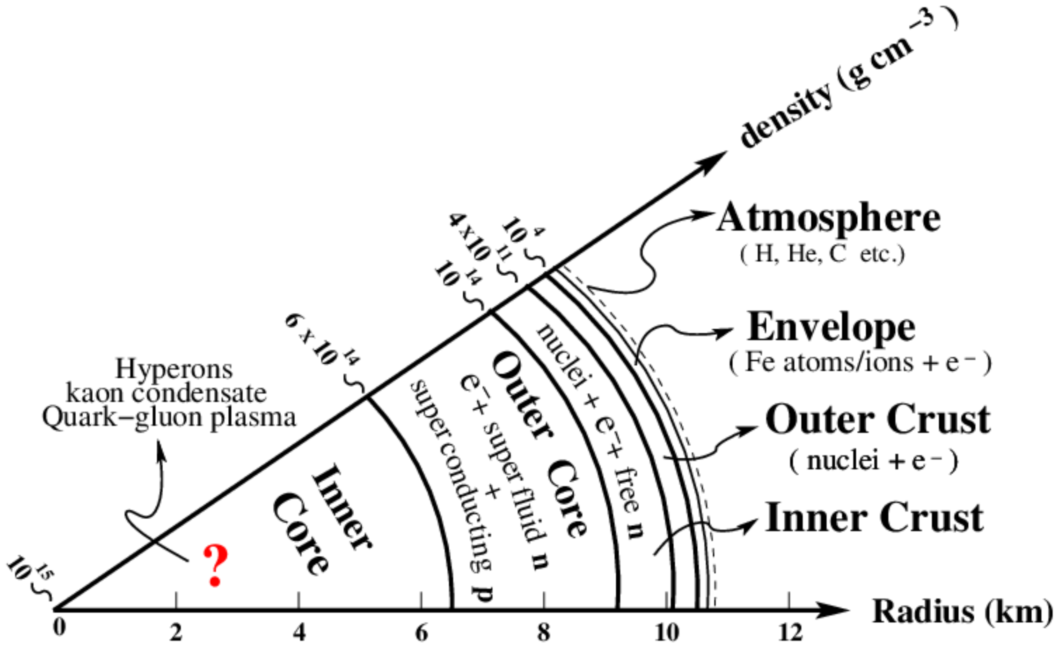

FIGURE 1.2: Schematic structure of a neutron star interior (Nandi and Bandyopadhyay, 2012).

- The inner crust, where neutron-rich nuclei, free neutrons and free relativistic electrons co-exist.
- The outer core, where the inverse beta decay occurs and we find mainly superfluid neutrons and small numbers of superconducting protons, relativistic electrons and muons, all in a degenerate state.
- The inner core, for which we know very little. Some exotic states of matter that have been proposed are quark-gluon plasma, hyperons, meson condensates, etc.

1.3.4 Energetics

Pulsars, unlike main sequence stars, do not produce energy . They are bright stellar corpses that slowly cool down. The total energy reserve is equal to the rotational[2]energy they acquired after the supernova explosion.

$$\varepsilon = \frac{I\Omega^2}{2} = \frac{2\pi^2 I}{P^2} \tag{1.2}$$

where P is the rotational period and I the star's moment of inertia. Therefore their luminosity can be estimated as the time derivative of the total stored energy.

$$\frac{d\varepsilon}{dt} = \mathcal{L}_{rot} = -\frac{4\pi^2 I\dot{P}}{P^3} \tag{1.3}$$

This is called the **pulsar spin-down luminosity**. We already mentioned that a pulsar can be modelled as a rotating, inclined magnetic dipole. From basic electromagnetism we know that such a dipole radiates and loses energy at a rate

[2]This is the most characteristic case but not the only one. The energy reserve of a pulsar can be of a different form as illustrated in sec. 1.5

$$P_{rad} = \frac{2}{3}\frac{m_B^2 \sin a^2 \Omega^4}{c^3} = \frac{2}{3c^3}(Br_*^3 \sin a)^2 \left(\frac{2\pi}{P}\right)^4 \tag{1.4}$$

where B is the magnetic field and r_* is the radius of the star.

Assuming that a pulsar is a perfect magnetic dipole (this is not the actual case, just a good approximation) and all the spin down luminosity is radiated away in the form of magnetic dipole radiation we can estimate the surface magnetic field as function of $M, r_*, P, \dot{P}$

$$\begin{aligned} \mathcal{L}_{rot} = P_{rad} \Rightarrow & \frac{4\pi^2 I\dot{P}}{P^3} = \frac{2}{3c^3}(Br_*^3 \sin a)^2 \left(\frac{2\pi}{P}\right)^4 \\ \Rightarrow & B_* = \sqrt{\frac{3c^3 MP\dot{P}}{20\pi^2 R_*^r \sin a}} \end{aligned} \tag{1.5}$$

The corresponding values are $B \simeq 10^{12}\ G$ and were calculated using known and observable quantities for pulsars.

In addition, we can estimate a **characteristic age** for pulsars. If the magnetic dipole moment does not change significantly during the pulsar's lifetime then from eq. 1.5 we get

$$P\dot{P} = \frac{8\pi^2 r_*^6 (B \sin a)^2}{3c^3 I} \tag{1.6}$$

which is constant. Therefore we have

$$\begin{aligned} P\dot{P} = P\frac{dP}{dt} = \mathcal{C} \Rightarrow & \int_{P_0}^{P} PdP = \mathcal{C}\int_0^\tau dt \\ \Rightarrow & \frac{P^2 - P_0^2}{2} = \mathcal{C}\tau \end{aligned} \tag{1.7}$$

But $\mathcal{C} = P\dot{P}$ and in the limit $P >> P_0$ we get

$$\frac{P^2}{2} = P\dot{P}\tau \Rightarrow \tau = \frac{P}{2\dot{P}} \tag{1.8}$$

where τ is the pulsar age. This is a simplified calculation. Nevertheless if we apply it to the Crab pulsar, the most famous and well studied pulsar in the entire population, the result is surprisingly close to its actual age. The Crab pulsar was created in A.D. 1054 during a massive supernova explosion that was observed and recorded by Chinese astronomers. Using the period $P = 0.033\ s$ and spin down $\dot{P} = 10^{-12.4}\ s/s$ of the Crab pulsar we find a characteristic age of $\tau \simeq 1300\ y$ which is an acceptable estimate given the crude assumptions we made.

1.4 Observations

Pulsars were originally detected in radiowaves and their study was considered a part of radio astronomy. With time and as the instrumentation evolved, observations in all other bands were carried out. As a result we now have a multiwavelength picture of pulsars spanning from radiowaves to γ -rays (fig. 1.3), which is crucial in our effort to understand the underlying physics behind them.

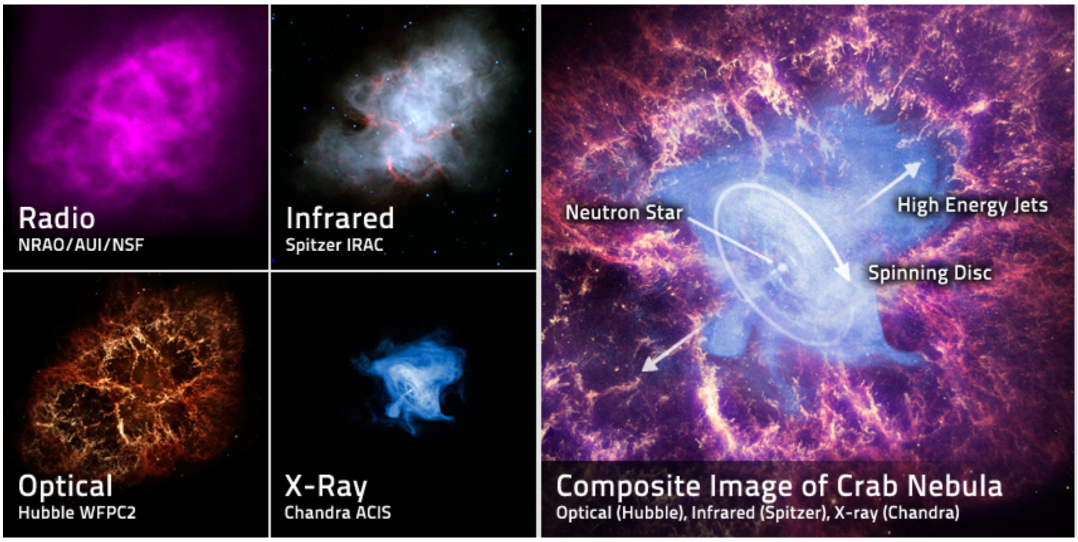

FIGURE 1.3: The crab nebula, with the crab pulsar in its centre in different wavelengths. The emission from the nebula is not pulsed as opposed to that of the pulsar.

1.4.1 Lightcurves

The light curves we obtain from pulsars in all wavelengths consist of very stable pulses with little to no radiation between them (fig. 1.4). This is a combined result of the pulsars rotation, the inclination between rotational and magnetic axes and the highly anisotropic emission and is called the **lighthouse effect**. For reasons that will be thoroughly explained in the next chapter, the region above the magnetic poles has the ability to accelerate particles in relativistic energies up to $\Gamma \simeq 10^7$. This can produce synchrotron emission of radiowaves, geometrically confined in a narrow cone just above the magnetic poles[3]. With that in mind, let's delve deeper into the emission pattern: as the pulsar rotates, the narrow cone circles around the rotational axis because of the inclination. When the cone crosses our line of sight we detect a pulse while in all other phases of the pulsar rotation we detect no radiation, similar to how a lighthouse is seen by a nearby ship. This is illustrated in fig. 1.5. Pulses in other bands can be explained using the same line of arguments, however the emission region and mechanisms can differ from those of the radio emission.

1.4.2 Spectrum

The observed spectra of pulsars give us extremely valuable information for their properties and structure. A typical spectrum covers all bands of electromagnetic radiation, from radio-waves to TeV γ - rays, but in some cases pulsars are quiet in certain bands. The lion's share of the radiated energy is carried by high-energy photons, namely X - rays and γ - rays with only a small portion going to radio-waves. In particular the high energy component consists of a power law followed by an exponential cutoff. The cutoff energies have a value of a few GeV. These features can be seen in the Crab pulsar spectrum in figure 1.6. The successful reproduction of the spectrum and light curves is the final judge of the various magnetospheric models found in literature.

[3] This is the general concept of radio emission, rather than a detailed description. There is strong evidence that the emission is radiated in the form of a cone, but the exact mechanism is still under investigation.

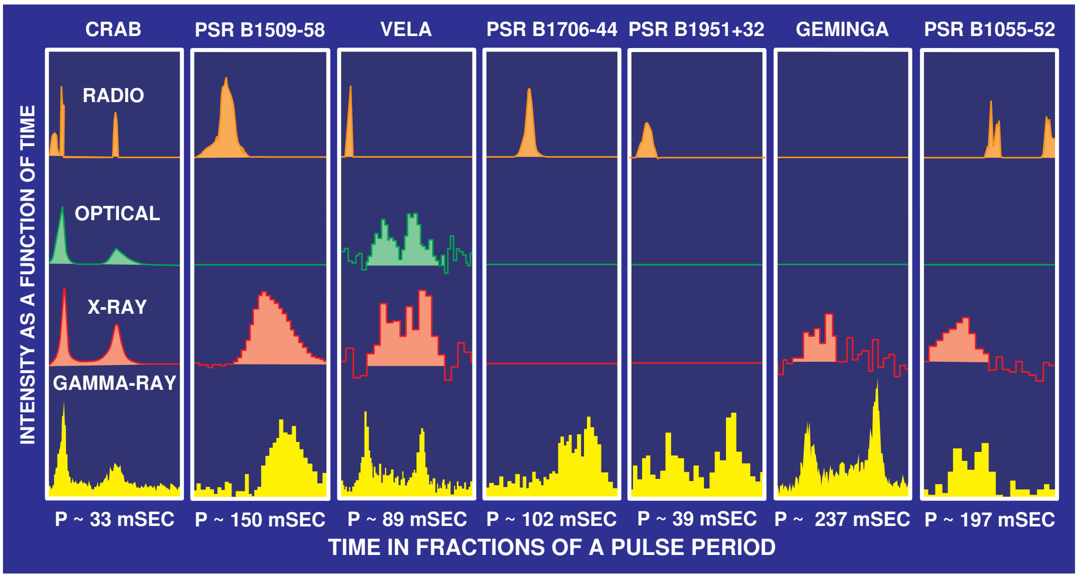

FIGURE 1.4: Multiwavelength lightcurves for seven pulsars

1.5 Population

The entirety of the pulsar population can be gathered and depicted in a $P - \dot{P}$ diagram, which has the pulsar period and period derivative as its axes (fig. 1.7). In this diagram, contours of the spin-down luminosity (or the magnetic field strength) and the pulsar's age can be drawn, which gives a general and informative overview of the known pulsars.

As with all the celestial objects, pulsars can be divided into a variety of categories. The most important classification depends on the origin of the energy that is radiated away (Harding, 2013). In this context we have:

1. Rotation-Powered Pulsars (RPP), where the energy comes from the rotation of the neutron star. They may be lone or in binary systems.

2. Accretion-Powered Pulsars. These are pulsars in binary systems that gain energy from the accreting matter of their counterpart.

3. Magnetars, pulsars with extremely high magnetic fields (up to $10^{15}G$). The energy source is the stored magnetic field energy.

4. Central Compact Objects (CCO). They are neutron stars located in the centre of supernova remnants with low magnetic fields. Their emission consist only of a thermal X-ray component, so they radiate away their stored thermal energy.

5. Isolated Neutron Stars (INS), similar to CCO but without a nebula surrounding them.

6. Rotating Radio Transients (RRT), a subpopulation of RPP that appear to 'turn off' for long periods of time.

All of these categories can be seen in $P - \dot{P}$ diagram (fig. 1.7) in different locations, indicative of their properties. The most important is the first category so it deserves some further discussion.

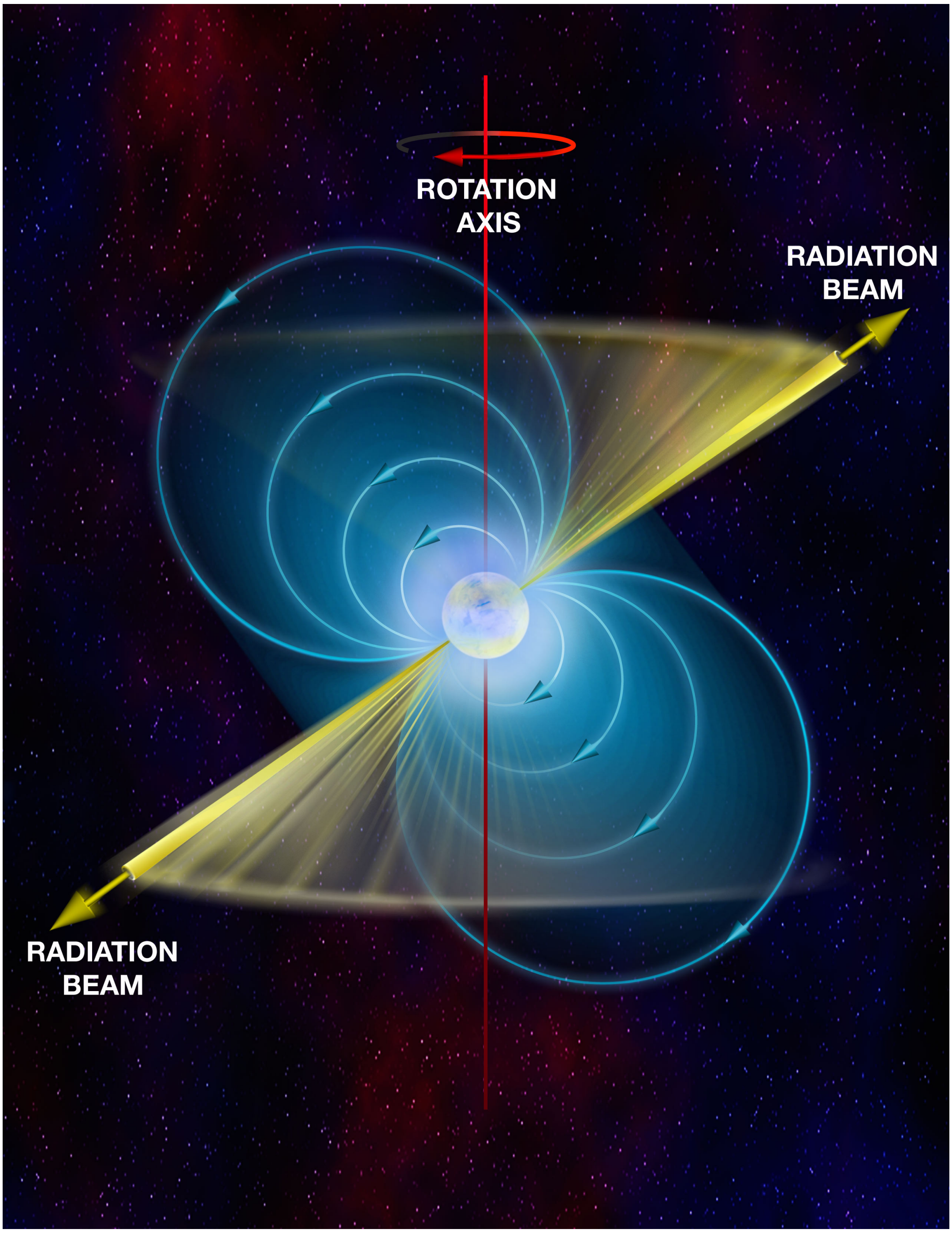

FIGURE 1.5: Graphic illustration of pulsar's magnetic field and radio emission

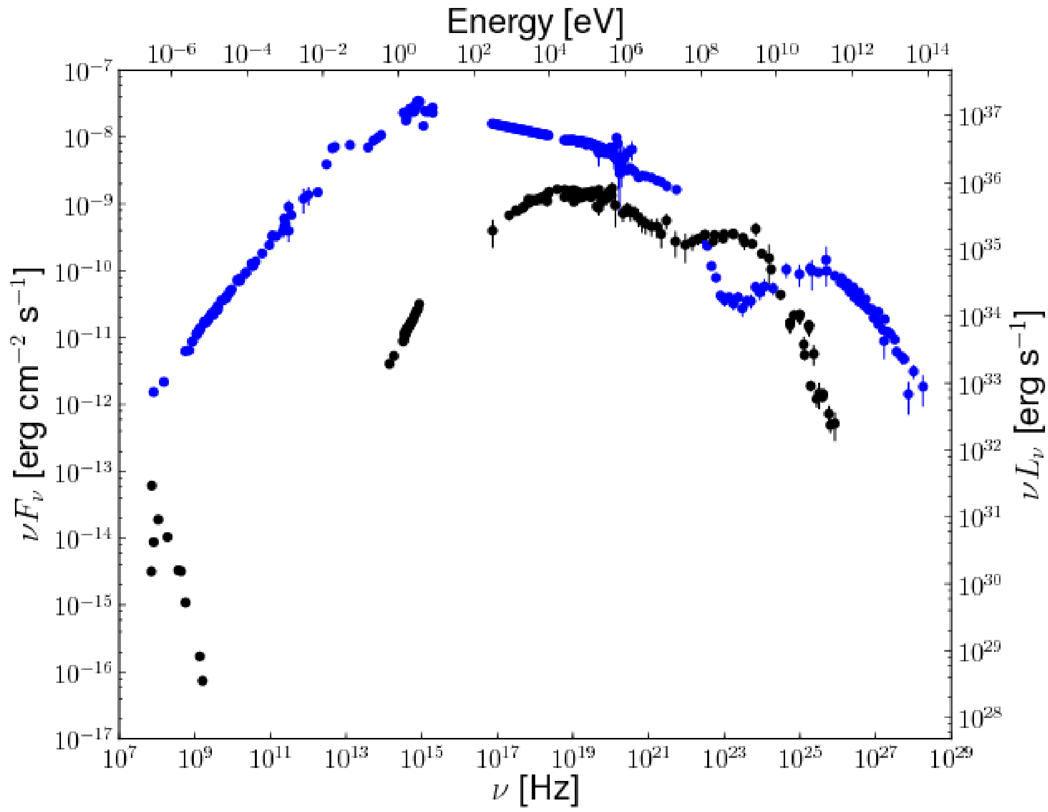

FIGURE 1.6: Spectral energy distribution of the average emission of the Crab nebula (blue) and the phase averaged emission of the Crab pulsar (black) (Bühler and Blandford, 2014).

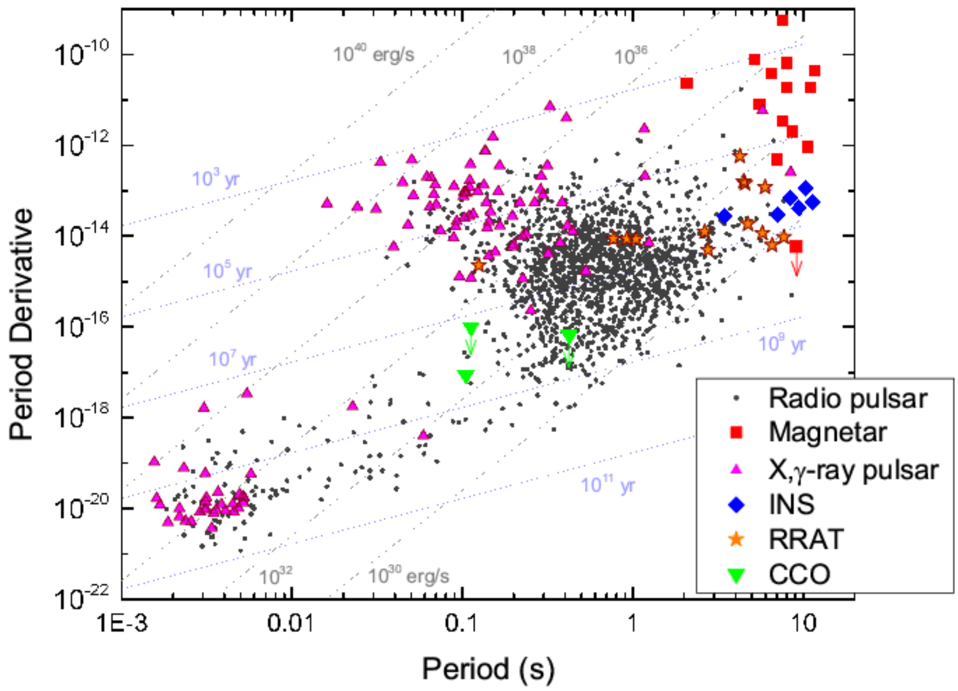

FIGURE 1.7: Plot of period vs. period derivative for the presently known rotation-powered pulsars, Isolated Neutron Stars (INS), Compact Central Objects (CCO), Rotating Radio Transients (RRATs) and magnetars (from `http://www.atnf.csiro.au/people/pulsar/psrcat/`). Lines of constant characteristic age, τ, and dipole spin-down luminosity, $\mathcal{L}_{sd}$, are superposed (Harding, 2013).

RPP can be divided in two main subclasses: normal RPPs and millisecond pulsars (MSP). The former can be found in the crowded central area of the $P - \dot{P}$ diagram and are generally what we have described in this chapter. MSPs cover the lower left region of the diagram. They are old pulsars ($\tau \geq 100\ Myr$) with short periods, which is an oddity because pulsars lose energy and slow down with age. They are probably 'recycled' old normal RPPs in binary systems. When the pulsar's companion star reaches the red giant phase and expands, matter falls into the pulsar, increases its angular momentum and accelerates it. Thus MSPs have low magnetic fields and spin-down due to age and short periods due to acceleration. For this thesis, a typical pulsar is a normal RPP. All the aspects discussed in this and the following chapters will be applied to this population unless stated otherwise.

Another interesting feature of RPPs is the occasional appearance of a sudden change in their period, namely a 'glitch' (fig. 1.8). This is a quick incident and the normal expected value of the rotational period is restored in a timescale of days or weeks. The exact cause of glitches is still unknown, but it is believed that is related to internal processes of the neutron star. Currently the general idea behind glitches is that the the crust of the neutron star is rotating slower than the superfluid core. An occasional coupling of the two transfers angular momentum from the core to the surface causing the glitch. Observing and studying glitches can give us a direct look to the neutron star interior and help us reveal some of the most elusive areas of condensed matter physics.

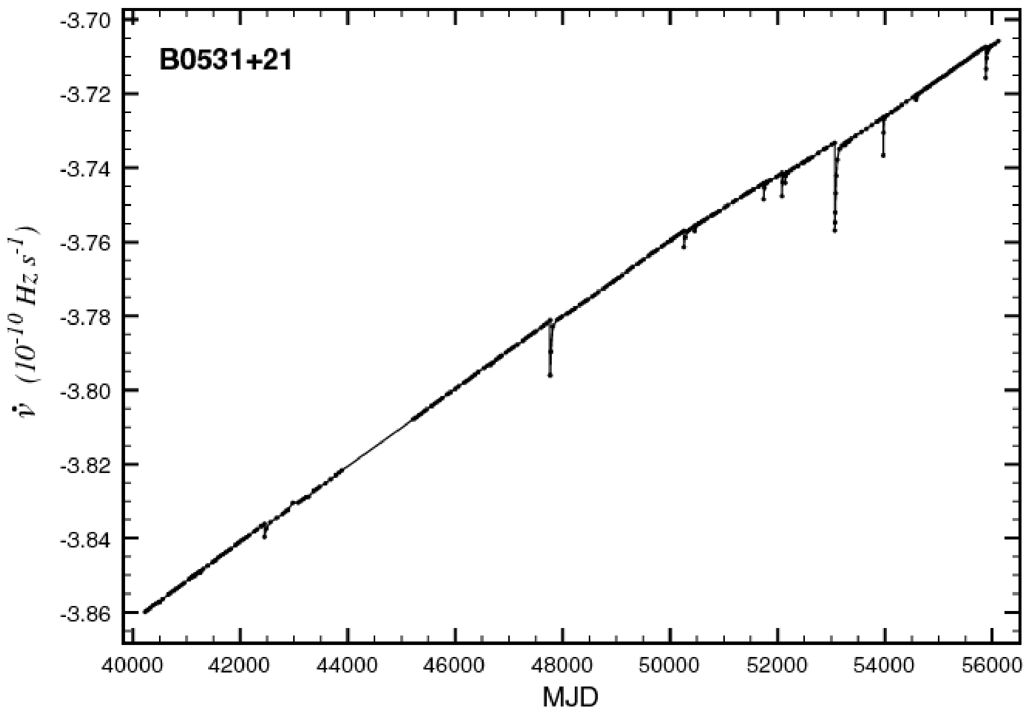

FIGURE 1.8: The $\dot{\nu}$ (where ν is the rotation frequancy) time-evolution of the Crab pulsar (PSR B0531+21) over more than 40 years (Espinoza, 2013)

1.6 Current Status

Presently, several positive developments, both observational and theoretical, have pushed our understanding of pulsars a bit further.

The Fermi era has really been a blessing for the study of high-energy emission, as the number of observed γ - ray pulsars has immensely augmented. To give a perspective, before the launch of Fermi only 7 pulsars had been confirmed to radiate in γ -rays while now we have a sample of more than 200. This allowed a statistical processing of the data and enforced restrictions to the models. Furthermore the recent discovery of gravitational waves and the ignition of the multimessenger era, pulsars can be seen with new eyes. Neutron stars are important objects in gravitational wave field because they can emit or used to detect gravitational waves. Although this does not directly relate with the high energy radiation it is certainly an important development with yet to be seen results.

On the theoretical side, the increased computational capacity has provided the opportunity to perform sophisticated pulsar simulations. Particle in Cell (PIC) simulations are an example. With this technique an 'ab initio' simulation can be performed which follows particle trajectories and their effect on the electromagnetic field until a stable condition is reached. This gives us a good qualitative picture of the pulsar but the downside is that such simulations are very expensive computationally and need several approximations to be implemented in order to generalise the results.

2 The Magnetosphere

2.1 Definition

The region surrounding an astrophysical object where charged particles interact with the object's magnetic field is called a **magnetosphere**. It is a region where plasma and magnetic field lines coexist and affect each other. Pulsars have extremely strong magnetic fields so it is only natural that they posses magnetospheres. All the emission processes (with the exception of thermal emission) take place in this region, therefore it is the most important and interesting feature of pulsars and the basis of what is examined in this thesis.

2.2 Formation

A magnetosphere can be created even if the area around a pulsar is initially empty, meaning that there is no plasma or charged particles, due to the fact that the electromagnetic forces are far stronger than gravity (Goldreich and Julian, 1969). This is illustrated below for the case of the aligned rotator.

We assume that the interior of the neutron star is a perfect conductor, $\sigma \to +\infty$. From Ohm's law we get:

$$\begin{aligned} \boldsymbol{J} &= \sigma(\boldsymbol{E}_{in} + \frac{\boldsymbol{v}}{c} \times \boldsymbol{B}_{in}) \\ \Rightarrow \boldsymbol{E}_{in} &= -\frac{\boldsymbol{v}}{c} \times \boldsymbol{B}_{in} \\ \Rightarrow \boldsymbol{E}_{in} &= -\frac{1}{c}\boldsymbol{\Omega} \times \boldsymbol{r} \times \boldsymbol{B}_{in} \end{aligned} \tag{2.1}$$

where $\boldsymbol{\Omega}$ is the star's angular velocity and $\boldsymbol{r}$ is the distance from the star's centre. This is the ideal magnetohydrodynamics (MHD) condition. The magnetic field in the interior has a dipole form, which is given in polar coordinates by:

$$\boldsymbol{B}_{in} = B_* \frac{r_*^3}{r^3} \left(2cos\theta \, \hat{\boldsymbol{r}} + \sin\theta \, \hat{\boldsymbol{\theta}} \right) \tag{2.2}$$

where B_* is the surface magnetic field at the magnetic equator and r_* is the star's radius. From eq. 2.1 and 2.2 we evaluate the electric field inside of the neutron star surface:

$$\boldsymbol{E}_{in} = \frac{B_* \Omega r_*^3}{2cr^2} \left(\sin^2\theta \, \hat{\boldsymbol{r}} - 2\cos\theta \sin\theta \, \hat{\boldsymbol{\theta}} \right) \tag{2.3}$$

and by integrating we get the electric potential inside of the neutron star's surface:

$$V_{in} = \frac{B_* \Omega r_*^3}{2cr} \sin^2\theta + C \tag{2.4}$$

The total charge of the neutron star must be equal to zero. Applying Gauss' s law we find $C = -\frac{B_* \Omega r_*^2}{3c}$

Now we calculate the the electric potential and the electric field outside of the neutron star by solving the Laplace equation in vacuum with the boundary condition $V_{in}|_{r=r_*} = V_{out}|_{r=r_*}$:

$$\begin{aligned}
&\nabla^2 V_{out} = 0 \\
&\Rightarrow V_{out} = \frac{B_* \Omega r_*^5}{6cr^3}(1 - 3\cos^2\theta) \\
&\Rightarrow \boldsymbol{E}_{out} = \nabla V_{out} = \frac{B_* \Omega r_*^5}{2cr^4}\left[(1 - 3\cos^2\theta)\,\hat{\boldsymbol{r}} - 2\sin\theta\cos\theta\,\hat{\boldsymbol{\theta}}\right]
\end{aligned} \tag{2.5}$$

It is evident from eq. 2.3 and 2.5 that there is an electric field discontinuity at $r = r_*$. This translates in a surface charge density $\sigma = \frac{1}{4\pi}(E_{out} - E_{in})$. The external electric field 2.5 exerts a force to these charges that greatly exceeds gravity, despite the compactness of the neutron star. The ratio of the electrostatic to the gravitational force is $\frac{F_{el}}{F_{gr}} \simeq 10^9$ for a proton, and even greater for an electron. Particles will be extracted from the surface and start filling the previously vacuum area around the star.

The strong electric field accelerates the particles in relativistic speeds while the strong magnetic field forces them to move along the field lines. Under these conditions particles can emit curvature radiation. With the Lorentz factors reaching values up to $\Gamma = 10^7$ the emitted photons are highly energetic and can be absorbed from the magnetic field creating electron-positron pairs.

$$\gamma + B \rightarrow e^- + e^+ \tag{2.6}$$

These pairs will then be accelerated from the electric field and emit synchrotron radiation which will be absorbed by the magnetic field and create a new generation of pairs and the this process will be perpetuated (see fig. 2.1). The result is a **cascade** of charged particles that will entirely fill the pulsar's surroundings and form a magnetosphere. Particles will be distributed through the magnetosphere in a polarised fashion, similar to a Faraday disk. In an aligned rotator positive charges will be gathered near the equator and negative charges will be gathered above the magnetic poles. As the charge density increases, the shape of the electromagnetic field deviates from the vacuum solution and the conductivity of the plasma goes to infinity. Gradually the component of the electric field that is parallel to the magnetic field lines $E_\parallel$ is screened because eq. 2.1 holds everywhere in the magnetosphere and not just inside the star. The pair creation efficiency decreases because there is no parallel electric field to accelerate the new particles to high enough energies. A stable state will be reached with a determined charge and current density distribution, electromagnetic field configuration and plasma flow. The dominant force is the electromagnetic. Gravity, plasma inertia and thermal pressure can all be neglected. This regime is called **Force Free Electrodynamics** (FFE).

Plasma in the magnetosphere is frozen in the magnetic field lines. Particles can only move along them and drift. This means that the magnetosphere rotates as a rigid body following the pulsar's rotation. This corotation ceases at a distance $R_{\ell c}$ where the plasma tangential speed $u = \Omega r$ would be equal to the speed of light c.

$$R_{\ell c} = \frac{c}{\Omega} \tag{2.7}$$

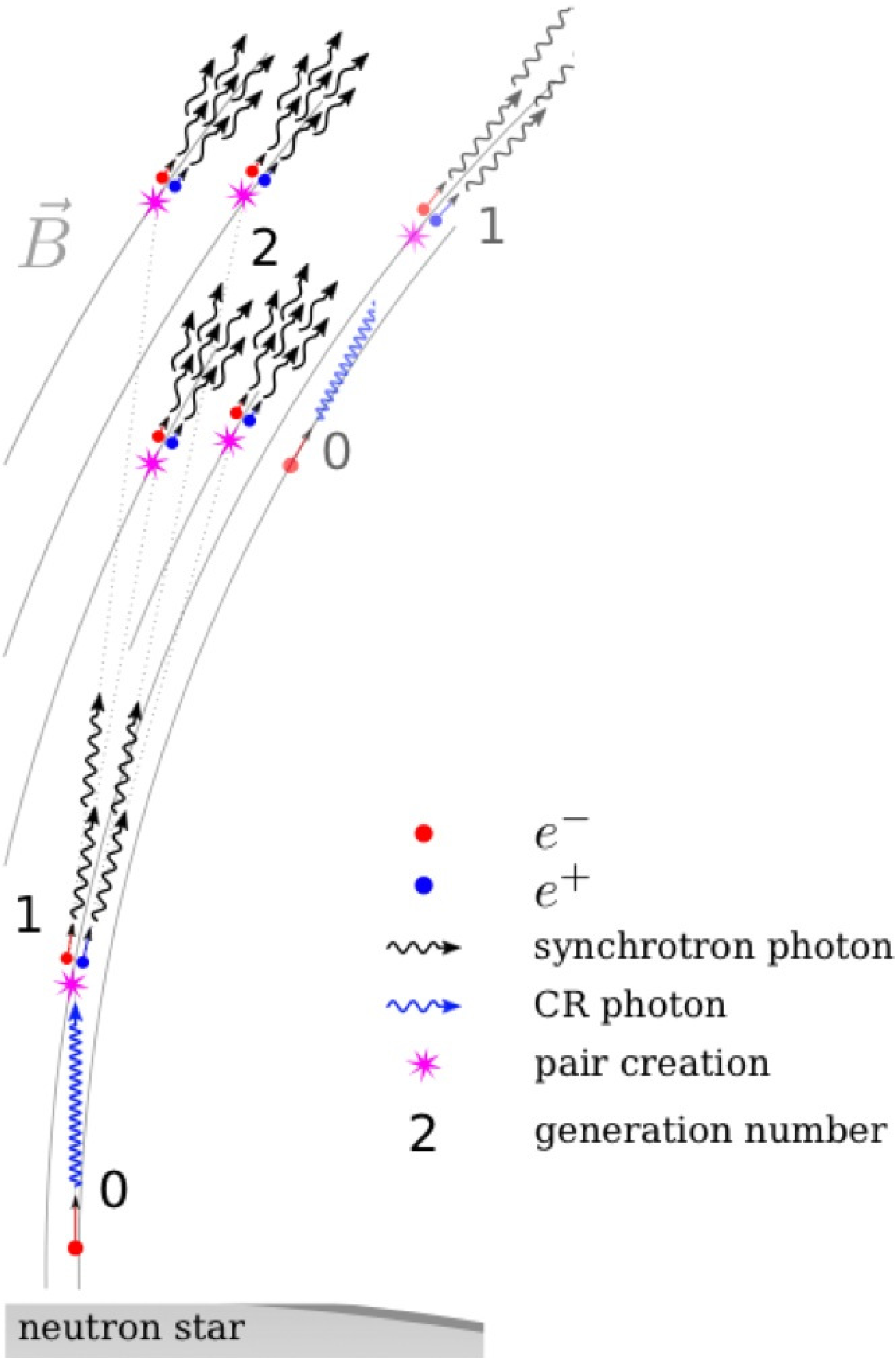

FIGURE 2.1: A schematic illustration of the electron-positron pair cascade above the polar cap (Timokhin and Harding, 2015).

The imaginary cylindrical surface with radius $R_{\ell c}$, whose axis coincides with the rotational axis of the pulsar is called **the light cylinder** (LC) and is one of the most important concepts about the magnetosphere.

Because plasma cannot corotate with the star outside of the light cylinder, the magnetic field lines that would close beyond it must break and bend in a direction opposite to the pulsar's rotation. This effect distinguishes two regions in the magnetosphere: 1) the **closed magnetosphere**, which lies entirely inside the LC and where all the magnetic field lines close without any problems, and 2) the **open magnetosphere** where all the magnetic field lines break and open up to infinity. The border between these two regions is called the **sepraratrix**. The region above the magnetic poles, where we can trace the footpoint of all the open field lines is called the **polar cap**.

In the closed magnetosphere (also called the dead zone), the particles are trapped, the parallel electric field is completely screened and there is no radiation. All the interesting phenomena occur in the open magnetosphere. The particles flow along the open field lines, cross the light cylinder and escape to infinity. They are then replenished by the $e^{\pm}$ pairs created in the polar cap (see sec. 2.3 for details). The parallel electric field is almost everywhere screened, with the exception of certain non ideal dissipative zones, which will be dealt with thoroughly, in the following sections.

As a final note, we need to clarify that this is not the most probable case. Pulsars are expected to have a magnetosphere from the beginning due to the fact that they are born within the particle-rich environment of a supernova explosion. Nevertheless the above analysis shows that even in the extreme case of a vacuum environment a magnetosphere will be created so we can safely assume that every pulsar has one. Furthermore, because particles flow through open magnetic field lines, the initial particle composition will be quickly replaced by electron positron pairs. For this reason it is generally assumed by the community that the magnetosphere consists of electron-positron plasma but a different composition cannot be excluded.

2.3 Gaps

In a stable magnetospheric condition, the ideal FFE regime dominates. The simplest case we can examine is an ideal, stationary, axisymmetric magnetosphere.

In FFE the total Lorentz force is equal to zero, so

$$\frac{\boldsymbol{J} \times \boldsymbol{B}}{c} + \rho_e \boldsymbol{E} = 0 \tag{2.8}$$

where $\boldsymbol{J}$ is the electric current density and ρ_e is the charge density and they are given by

$$\begin{aligned} \boldsymbol{J} &= \frac{c}{4\pi} \nabla \times \boldsymbol{B} \\ \rho_e &= \frac{\nabla \cdot \boldsymbol{E}}{4\pi} \end{aligned} \tag{2.9}$$

The electric field can be written as

$$\boldsymbol{E} = \frac{R\Omega}{c} \boldsymbol{B}_p \times \hat{\boldsymbol{\phi}} \tag{2.10}$$

The smartest way to proceed is to express the magnetic field in terms of the flux function Ψ and use cylindrical coordinates (R, ϕ, z)

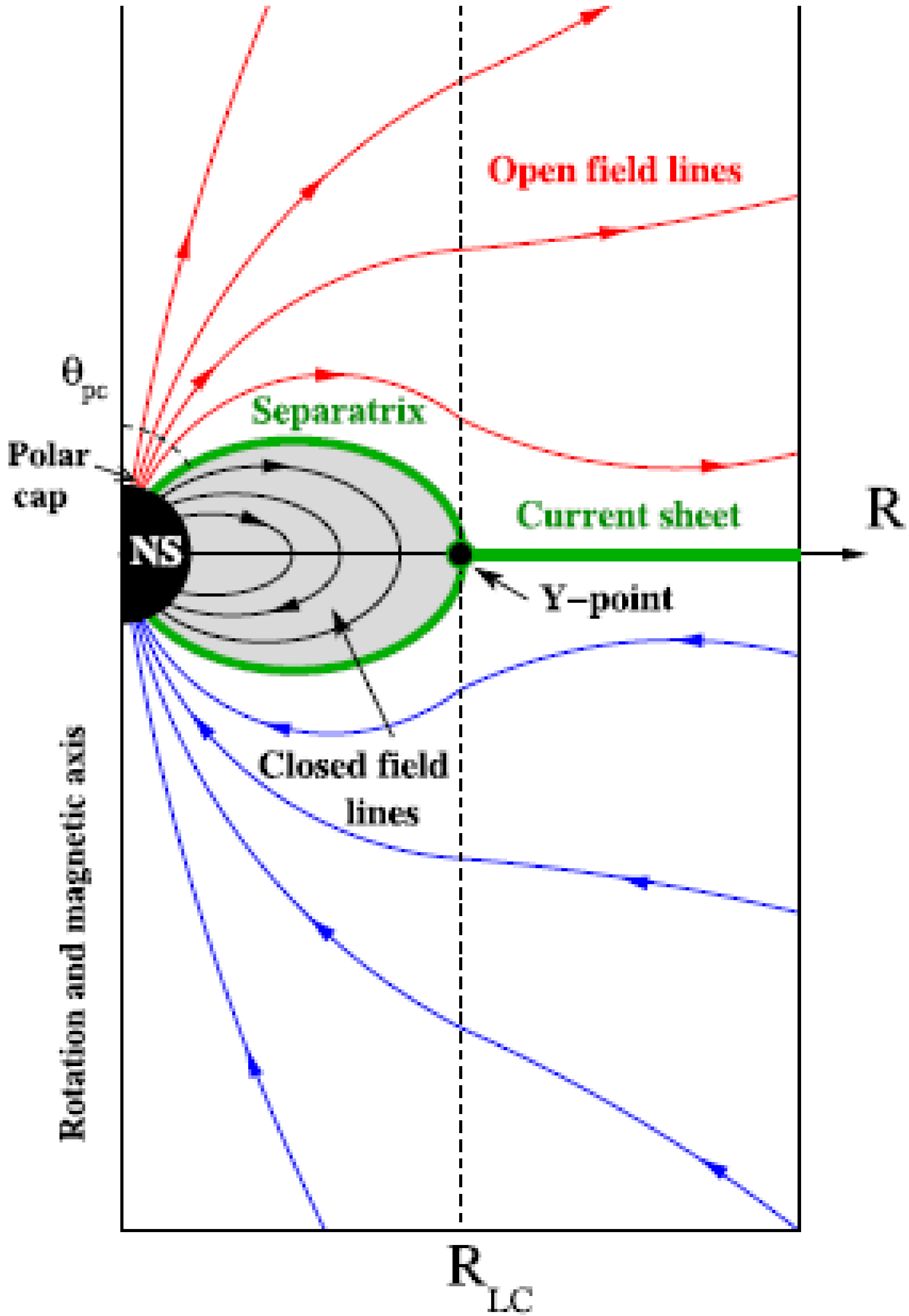

FIGURE 2.2: Sketch of the ideal force-free magnetosphere of the aligned pulsar. The main elements are: (i) The closed field line region (grey, and black field lines) lying between the star surface and the light cylinder. This zone is dead and does not participate to the pulsar activity. (ii) The open field line region (red and blue field lines) extending beyond the light cylinder. The open field-line bundle carries the outflowing electric current, Poynting flux and the relativistic pulsar wind. (iii) The equatorial current sheet (green) between the opposite magnetic fluxes in the wind zone. It splits at the light cylinder into two separatrix current sheets that go around the closed zone, between the last open and the first closed field lines (Cerutti and Beloborodov, 2017).

$$\begin{aligned} B_p &= \frac{\nabla\Psi \times \hat{\boldsymbol{\phi}}}{R} \\ B_\phi &= \frac{A(\Psi)}{R}. \end{aligned} \tag{2.11}$$

where $A \equiv \frac{2I}{c}$ and I is the poloidal electric current. Now we can rewrite eq. 2.8 in terms of Ψ as

$$(1-x^2)\left(\frac{\partial^2\Psi}{\partial x^2} + \frac{\partial^2\Psi}{\partial Z^2}\right) - \frac{1+x^2}{x}\frac{\partial\Psi}{\partial x} = -R_{\ell c}^2 A(\Psi)A' \tag{2.12}$$

where $x = \frac{R}{R_{\ell c}}$ and $Z = \frac{z}{r_{\ell c}}$. This is known as the **pulsar equation** and was first derived by (Michel, 1973; Scharlemann and Wagoner, 1973). This equation does not have an exact general analytical solution. It was first solved numerically by (Contopoulos, Kazanas, and Fendt, 1999) and thereafter by many other authors.

If the pulsar equation is satisfied, the charge density is given by

$$\rho_e = \left(\frac{\Omega}{4\pi c}\right)\frac{-2Bz + AA'}{1-x^2} \tag{2.13}$$

which is better known as the **Goldreich-Julian charge density** ρ_{gj}. Near the star's surface where $x \ll 1$ the expression becomes

$$\rho_{gj} \simeq -\frac{\boldsymbol{\Omega}\cdot\boldsymbol{B}}{2\pi c} \tag{2.14}$$

This expression was derived by (Goldreich and Julian, 1969)[1]in their pioneering work on pulsar magnetospheres. From this expression we can see that there are regions with positive charge density, where $\boldsymbol{\Omega}\cdot\boldsymbol{B} < 0$ and regions with negative charge density, where $\boldsymbol{\Omega}\cdot\boldsymbol{B} > 0$, as well as a surface with zero charge density, where $\boldsymbol{\Omega}\cdot\boldsymbol{B} = 0 \Rightarrow \boldsymbol{\Omega} \perp \boldsymbol{B}$. This is called the **null surface** and is the border between the oppositely charged regions.

If, for any reason, there is a deviation of the local charge density from ρ_{gj} the parallel component of the electric field will not be completely screened. Such regions are called **gaps**. Gaps can operate as accelerators and as a result they are regions that can generate non-thermal emission. The idea of a magnetospheric gap acting as a particle accelerator was one of the earliest concepts about pulsars. For many years it was believed that this was the mechanism that channelled the pulsar' s energy to the particles and produced the non thermal radiation.

An important example is the **polar cap gap** (see fig 2.3). It occurs directly above the polar cap and close to the neutron star's surface, where a charge deficit is easy to appear. Charges can be extracted from the surface at a specific rate, depending on the magnitude of the electromagnetic force. This rate must be high enough to sustain the Goldreich-Julian charge density by replenishing the charges that flow through the open field lines. If this is not the case, the ideal MHD condition breaks and we have the formation of a gap. What stops the gap from extending all the way to infinity is the eventual screening of the electric field from the pair cascade created by the primary accelerated particles. At a certain height above the star's surface,

[1]The exact relationship that (Goldreich and Julian, 1969) found was $\rho_{gj} = \frac{-\boldsymbol{\Omega}\cdot\boldsymbol{B}}{2\pi c}\frac{1}{1-x^2}$. The difference is that they did not acount for the poloidal current an assumed that the current density is purely azimuthial.

where the cascade is initiated, a pair formation front is developed and marks the upper boundary of the gap.

The polar cap gap is the prime candidate for the source of the pulsar's radio emission. Unabsorbed synchrotron radiation coming from a narrow region above the magnetic poles can explain all the observational features of pulsed radio signals. On the other hand the observed high energy radiation cannot originate from the polar cap for two reasons: Firstly, the radio and the high energy component of the signal arrive at the observer with a phase delay between them. This implies that the location from which each component is emitted must be different. Secondly, with the launch of the Fermi LAT and the significantly increased number of pulsars observed, it was concluded that the high energy spectrum has a simple exponential cutoff in γ - rays. This is contradicting with emission from the polar cap because the strong magnetic field near the surface would absorb the high energy photons, resulting in a super exponential cutoff. This last point is important because it strongly constraints the topology of the high energy emission. It places its source in the outer magnetosphere, in the vicinity the LC or beyond.

Other gap examples are the outer gap, which can be formed in the region between the null surface and the light cylinder and the slot gap which is a narrow slice directly above the separatrix and extends from the polar cap to the outer magnetosphere (see fig 2.3). These gaps are compatible with the simple exponential spectral cutoff and were traditionally considered to host the high energy emission. However this idea is becoming less popular in recent years for a number of reasons. Gap models have failed to adequately reproduce the observational features and in addition suffer from theoretical inconsistencies about the formation and location of the gap. The modern picture of the magnetosphere favours another type of accelerator, based on magnetic dissipation. Overall, the existence of some or all forms of gaps cannot be decisively excluded, but it is highly unlikely that they are behind the high energy radiation.

2.4 Current Closure

One final issue regarding the magnetosphere is the need for current closure. The current that leaves the neutron star, carried by the particles that flow from the polar cap, must return back to the star. The magnetosphere is a large scale electric circuit, fed by the star and it is necessary that this circuit somehow closes in order to keep the pulsar neutral.

In the first successful simulation of an aligned, axisymmetric pulsar's magnetosphere Contopoulos, Kazanas and Fendt (Contopoulos, Kazanas, and Fendt, 1999) showed that only a small portion of the total polar cap current closes inside the polar cap itself. The bulk of the current returns to the star in the form **current sheets**.

Current sheets develop where there is a discontinuity in the magnetic field. In particular, there are two such regions in the magnetosphere. The first is along the magnetic equator, where the azimuthial magnetic field changes sign. The electric field is perpendicular to the magnetic field and points away from the current sheet. Therefore this **equatorial current sheet** (ECS) must be positively charged and the particles must move outwards. The second is a **separatrix current sheet** (SCS), because in the closed magnetosphere the magnetic field is purely poloidal while in the open magnetosphere has both a poloidal and an azimuthial component. We can quantify this by using the electromagnetic pressure. At the separatrix, the pressure

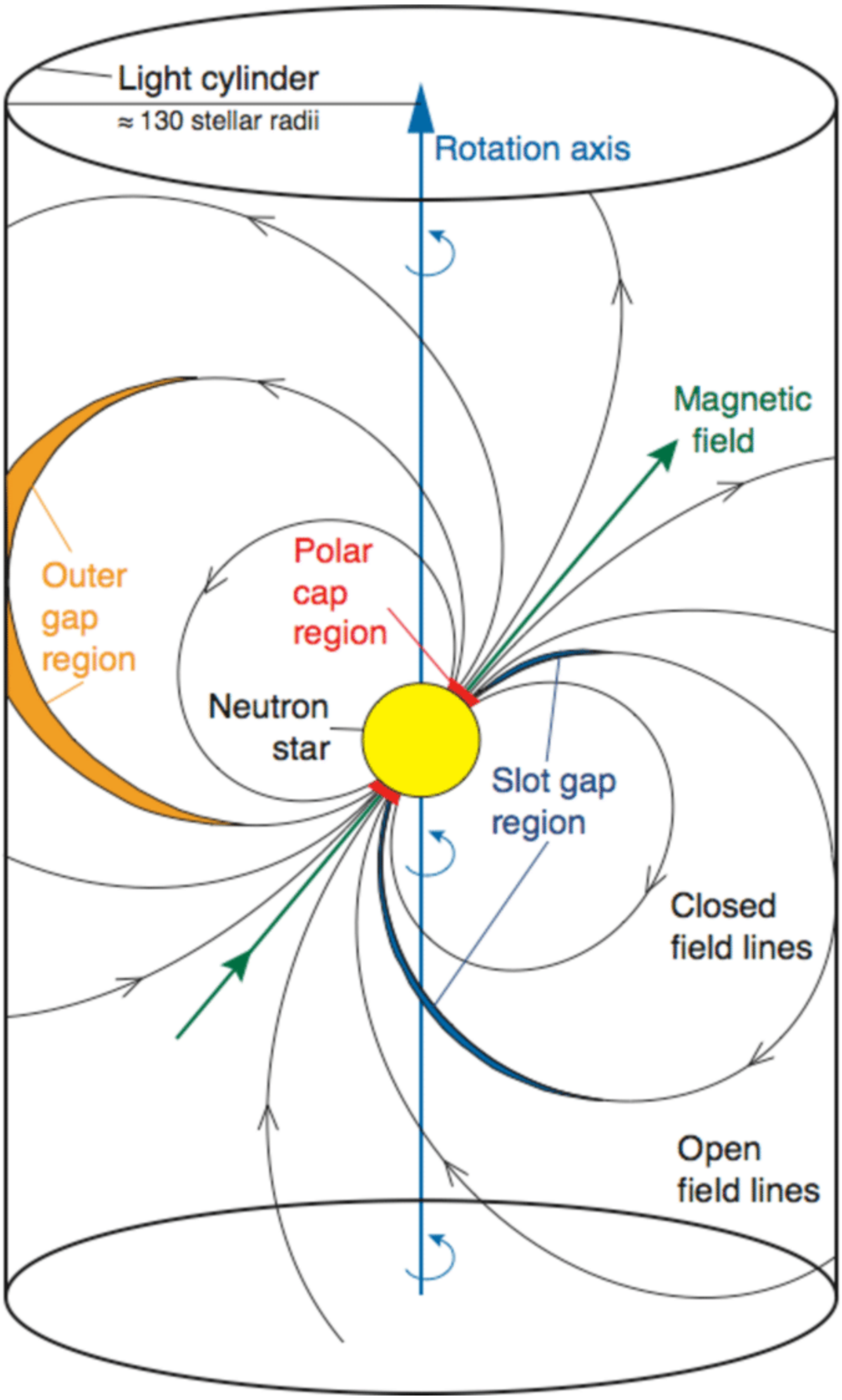

FIGURE 2.3: A sketch of a pulsar's magnetosphere with the possible locations of gaps (E et al., 2008).

in the closed magnetosphere must be equal to the pressure in the open magnetosphere

$$\begin{aligned} &B_{in}^2 - E_{in}^2 = B_{out}^2 - E_{out}^2 \\ \Rightarrow &B_{pol,in}^2 - E_{pol,in}^2 = B_{pol,out}^2 + B_{\phi,out}^2 - E_{pol,out}^2 \end{aligned} \tag{2.15}$$

Here the subscript 'in' means in the closed magnetosphere. From Ohm's law the poloidal electric field is simply $E_{pol} = \frac{r\sin\theta}{R_{\ell c}} B_{pol} = \frac{R}{R_{\ell c}} B_{pol} = x B_{pol}$, R being the cylindrical radius, so the above equation becomes

$$(1 - x_{in}^2) B_{pol,in}^2 = (1 - x_{out}^2) B_{pol,out}^2 + B_{\phi,out}^2 \tag{2.16}$$

But $x_{in} \simeq x_{out}$ and therefore $B_{pol,in} \neq B_{pol,out}$. If we solve for the electric fields we get

$$E_{pol,in}^2 - E_{pol,out}^2 = \frac{x^2 B_\phi^2}{1 - x^2} \tag{2.17}$$

This implies that the poloidal electric field is not continuous at the separatrix and the total electric field points towards the separatrix current sheet. There is a negative surface charge density that supports the discontinuity. In order to conform with the needed direction of the current, particles must move inwards at the speed of light.

The intersection point of the two current sheets is expected to be at or at least close to the light cylinder and is called the **Y-point** (see fig 2.2). An this point the current sheet surface charge density is expected to be equal to zero in order to permit the transition from a negative SCS to a positive ECS.

Current closure is a very important aspect of the theory of pulsar magnetosphere. We will show next that satisfying this constrain gives rise to a bunch of interesting concepts and ideas that go hand in hand with the high energy emission.

3 The 'Ring of Fire' Model for High Energy Emission

3.1 Motivation

As it was briefly mentioned in section 1.6, the latest methods in determining the magnetospheric structure involve global PIC simulations. In these simulations individual particles are followed as opposed to MHD simulations where a fluid is considered. The electromagnetic field configuration and the distribution of charge and current density are calculated in conjunction with each other. Regions of magnetic dissipation and particle acceleration naturally emerge and this pinpoints the origin of high energy emission. Furthermore, because the particle trajectories are known, it is possible to calculate high energy spectra and light curves and compare with the observations.

The problem with PIC simulations is the computational resources they require. Even the most advanced supercomputers are unable to reach the desired resolution and particle number. Limited resolution leads to numerical dissipation that cannot always be distinguished from the physical magnetic dissipation. Limited number of particles forces the use of super-particles with unrealistically high mass and charge and low Lorentz factors and multiplicities. Meanwhile, it is generally assumed that magnetic dissipation and particle acceleration only take place at the current sheets and the rest of the magnetosphere is force-free. A force free magnetosphere can be very easily reproduced by an MHD simulation. The only areas that should be of interest are the non-ideal current sheets and all the computational effort should be concentrated there.

On the other hand, in section 2.4 we emphasised that the current sheets are the links that ensure current closure in the pulsar magnetosphere. Their charge and current densities are determined by the needs of the global solution. The open question then is, what is the origin of these charge carriers. Numerical simulations cannot give us an adequate answer because particles are freely provided according to the needs of the solution. There is no limit on the number of available particles and no restrictions on the place of origin, therefore there is not a direct physical association between the reserve of charged particles and their distribution in the current sheets.

The semi-analytical model that will be described in this chapter attempts to solve simultaneously and with the minimum number of assumptions both issues:

1. The particle acceleration and high energy emission mechanism.

2. The source of the charge carriers that form the current sheets and the return current.

It is essentially a local study of the behaviour of charged particles in the vicinity of the magnetospheric Y-point. The aim of this approach is to build a general, self-consistent and theoretically robust picture of the magnetosphere before investing in global simulations.

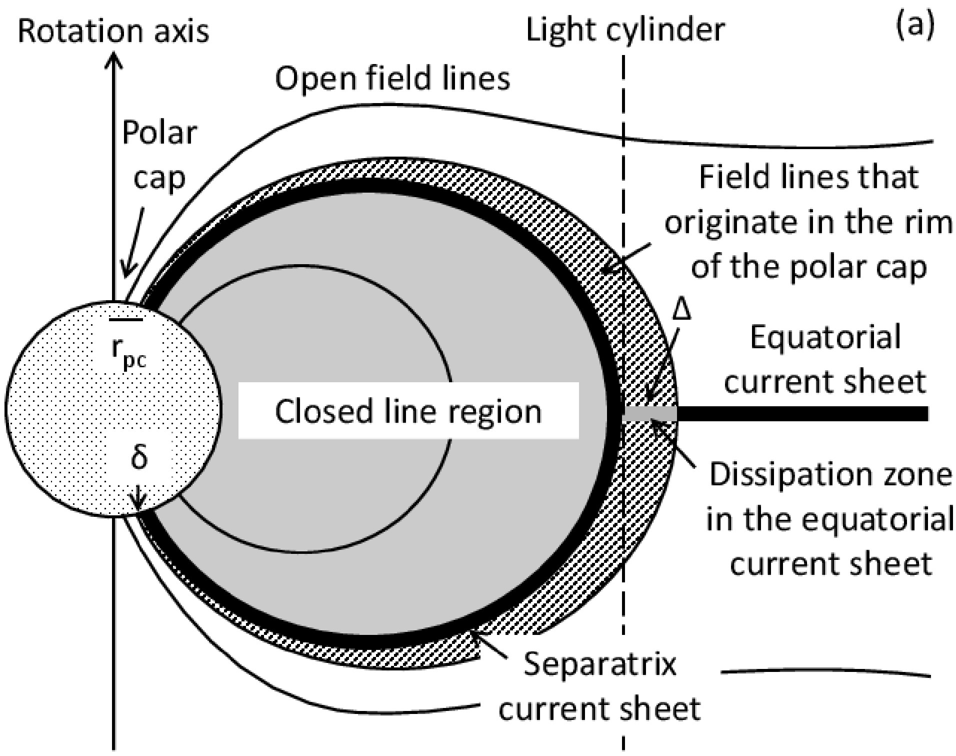

FIGURE 3.1: A schematic illustration of the dissipation zone. Central sphere: neutron star. Dashed line: light cylinder. Grey region: closed field lines. White region: open field lines. Striped region: field lines that originate in the rim of the polar cap and close in an equatorial dissipation zone (thick grey line) just outside the light cylinder. Thick black line: Return current sheet on the surface of and outside the striped region(Contopoulos, 2019)

3.2 Model Description

3.2.1 The dissipation zone

Our model relies heavily on the the ideas presented in (Contopoulos, 2019). We consider the magnetosphere to be everywhere ideal and force-free, apart from two regions: the gap above the polar cap where pairs are created and a narrow **dissipation zone** (DZ) on the ECS just outside the LC. The polar cap gap has already been explained on sec. 2.3 so we will elaborate on the the dissipation zone, which is our main concern.

By the term dissipation we mean conversion of magnetic field energy to particle energy through magnetic reconnection. Dissipative regions are by definition non ideal, therefore eq. 2.1 is not valid, the particles are not forced to move along magnetic field lines and the parallel electric field is not completely screened. As a result a portion of the field lines that originate from the polar cap are able to enter the ECS and close even in distances greater than $R_{\ell c}$ (see fig. 3.1). The footpoints of these lines are located in **polar cap rim**. The exact percentage of the open field lines that enter the ECS and the resulting width of the DZ depends on the **multiplicity** k, that is the number of particles created from each primary particle in the polar cap pair cascade.

The total electric current that flows from the polar cap is

$$I_{pc} = \rho_{gj} c \pi R_{pc}^2 \tag{3.1}$$

where

$$R_{pc} \simeq \left(\frac{r_*^3}{R_{\ell c}} \right)^{1/2} \tag{3.2}$$

is the polar cap radius and r_* is the radius of the star. The bulk of this current returns to the star through the separatrix current sheet, with just a small portion returning inside the polar cap rim. The current circuit of the pulsar can be written as

$$I_{pc} = I_{rim} + I_{sep} \tag{3.3}$$

Suppose that the polar cap rim is a ring in the edge of the polar cap of radius $R_{pc} - \delta < R < R_{pc}$. The magnetic field lines that originate from the rim carry a total pair flux of $F = 2\pi R_{pc} \delta k \rho_{gj} c/e$. These pairs enter the dissipation zone and they are accelerated by the parallel electric field. Electrons are accelerated inwards, towards the Y-point and then enter the separatrix current sheet. Positrons are accelerated outwards and fill the equatorial current sheet. The particle flux from the polar cap rim is channelled to the current sheets and supports the return current. A relation between the width of the rim and the pair multiplicity directly emerges:

$$\delta = \frac{I_{sep}}{k R_{pc} \Omega B_*} \tag{3.4}$$

where B_* is the magnetic field strength near the surface of the star. This is the width that the polar cap needs to have in order to provide the necessary amount of charge carriers to the current sheet given a specific multiplicity. In young, energetic pulsars the pair creation efficiency is expected to be very high so $k \gg 1$ and consequently $\delta \ll R_{pc}$ and $I_{pc} \simeq I_{sep}$. We may consider that the current closes entirely through the separatrix. By substituting the last relation in eq. 3.4 we get

$$\delta \simeq \frac{R_{pc}}{2k} \tag{3.5}$$

The magnetic flux that flows from the polar cap rim is conserved up to the dissipation zone so

$$\begin{aligned}
&B_* \pi [R_{pc}^2 - (R_{pc} - \delta)^2] = B_{\ell c} \pi [R_{\ell c}^2 - (R_{\ell c} - \Delta)^2] \\
\Rightarrow &B_* (2R_{pc}\delta - \delta^2) = 2B_* \left(\frac{r_*}{R_{\ell c}} \right)^3 (2R_{\ell c}\Delta - \Delta^2) \\
\Rightarrow &R_{pc}\delta \simeq 2R_{\ell c}\Delta \left(\frac{r_*}{R_{\ell c}} \right)^3 \\
\Rightarrow &\Delta \simeq \frac{R_{\ell c}}{2k}
\end{aligned} \tag{3.6}$$

where Δ is the the width of the DZ. In the above calculation we used eq. 3.2, 3.5, we neglected the squared terms because they are considered small and we assumed that the magnetic field always has a dipole form. Equation 3.6 is very important because it determines the DZ width as a function of the multiplicity, which is a free parameter in our model. Furthermore it shows that Δ is inversely proportional to k. This a reasonable result because the higher the multiplicity, the closer the magnetosphere is to the ideal FFE solution so the dissipation region is expected to be small. We will focus on high multiplicities $k \sim 10^3$ corresponding to young and active pulsars. For this reason we name our model the **'Ring of Fire'** (Contopoulos and Stefanou, 2019).

Lastly, a detailed discussion needs to be done for the thickness of the DZ and the current sheets in general. We will do this in terms of the half height h. Mathematically, current sheets are completely laminar, they represent an infinitely small discontinuity. In reality they must posses some thickness in order to secure a steep but smooth change in the magnetic field. The half height of the current sheet is determined by the orbit of the charge carriers. We will show, in sec. 5.1 that in the DZ the particles follow so called "Speiser orbits", i.e. gyrating orbits that become more and more stretched and compressed towards the equatorial plane. A good approximation is to consider as half-height the mean value of the gyroradius of particles at the moment of their injection to DZ. After their injection the compression of the orbit is very fast and the particles are confined near the equatorial plane so h is completely determined by the newly injected particles. If we consider a steady flow of particles with a steady mean gyroradius then we can safely estimate the DZ half-height as

$$h = \frac{\langle \Gamma_{inj} \rangle mc^2}{eB_{\ell c}} \tag{3.7}$$

where B_{lc} is the magnetic field in the light cylinder. For distances $R > R_{\ell c} + \Delta$ out of the DZ the current sheet is expected to be significantly thinner.

We note that the implementation of the correct value of h is very important because it affects the overall trajectory and the emission from the particles. A self consistent calculation can be done by statistically adding all the particle orbits that enter it at all radii. This is beyond the purposes of this work for which we find the approximation 3.7 adequate.

3.2.2 The local E/M field

The DZ is on the equatorial plane, very close to the LC and relatively small in size. We are interested in a local analysis so we will focus on an imaginary box around the DZ. There are three separate regions where the E/M field has different configuration (Contopoulos and Stefanou, 2019). We will describe these regions using cylindrical coordinates.

The first and most important is the DZ which is defined as the region in the interval $R_{\ell c} < R < R_{\ell c} + \Delta$. The electromagnetic field is:

$$\begin{aligned}
B_z &= -B_{\ell c} \\
B_\phi &= \begin{cases} -\frac{z}{h} B_{\ell c} & , z \le |h| \\ -sign(z) B_{\ell c} & , z > |h| \end{cases} \\
E_R &= |B_z| \frac{R}{R_{\ell c}} \\
B_R &= E_z = E_\phi = 0
\end{aligned} \tag{3.8}$$

For simplicity we consider that the field lines penetrate the DZ perpendicularly, so the poloidal field has only a z - component and that B_z is constant along the DZ and of the order of $B_{\ell c}$. The azimuthial component of the magnetic field must gradually change sign in the ECS - we chose linear function but another monotonous function can be chosen - but everywhere else is constant and of the order of $B_{\ell c}$. The electric field that accelerates the particles has only a radial component given by the well-known force free expression.

Outside of the right boundary of the DZ, where $R > R_{\ell c} + \Delta$, lies the dissipationless ECS. In this region the azimuthial magnetic field dominates so

$$
\begin{aligned}
B_\phi &= \begin{cases} -\frac{z}{h} B_{\ell c} & , z \leq |h| \\ -sign(z)\ B_{\ell c} & , z > |h| \end{cases} \\
B_R &= B_z = E_R = E_z = E_\phi = 0
\end{aligned}
\tag{3.9}
$$

Outside of the boundary between the DZ and the closed magnetosphere (or inside the closed magnetosphere), where $R < R_{\ell c}$, there is no azimuthial magnetic field. The poloidal field though is significantly augmented because of compressed magnetic flux. This abrupt increase is a relativistic feature related to the presence of the separatrix electric current near the light cylinder where $|E_R| \to |B_z|$, and involves only a rearrangement of the magnetic flux at the tip of the closed magnetosphere. Therefore we have

$$
\begin{aligned}
&B_z \gg B_{\ell c} \\
&E_R = B_z \frac{R}{R_{\ell c}} \\
&B_R = B_\phi = E_z = E_\phi = 0
\end{aligned}
\tag{3.10}
$$

Now that we have drawn he picture of the local E/M field we are in a position to construct the equations that describe the motion of charged particles.

3.3 Equations of Motion

In order to determine the particle trajectories we need to solve the relativistic momentum equation in tree dimensions using cylindrical coordinates. Cylindrical coordinates are the most suitable for an axisymmetric problem such as the one we are studying here. We will write down the equations in terms of the spacial component of the 4-velocity

$$\boldsymbol{u} = \Gamma \boldsymbol{v} \tag{3.11}$$

in order to avoid numerical setbacks that appear when 3-velocities approach the speed of light. The forces that act on the particles are the **E/M Lorentz force**

$$\boldsymbol{F}_{EM} = e\left(\boldsymbol{E} + \frac{\boldsymbol{v}}{c} \times \boldsymbol{B}\right) = e\left(\boldsymbol{E} + \frac{\boldsymbol{u}}{\Gamma c} \times \boldsymbol{B}\right) \tag{3.12}$$

and the **radiation reaction force**, which is the recoil exerted on the particles when they emit radiation

$$\boldsymbol{F}_{rad} = \frac{P_{rad}}{c^2}\boldsymbol{v} = \frac{P_{rad}}{\Gamma c^2}\boldsymbol{u} \tag{3.13}$$

where P_{rad} is the power radiated by particles that follow a curved trajectory

$$P_{rad} = \frac{2e^2 c \Gamma^4}{3R_c^3} \tag{3.14}$$

and R_c is the radius of curvature of the particle trajectory

$$R_c = \frac{|\boldsymbol{v}|^3}{\left|\boldsymbol{v} \times \frac{d\boldsymbol{v}}{dt}\right|} \tag{3.15}$$

in terms of the 3-velocity and 3-acceleration. We chose the general expression of curvature radiation because the orbit is rather complicated and we cannot predict which part will dominate. In that sense we do not distinguish between synchrotron and curvature radiation.

We must note here that eq. 3.13 is not trivial. The full expression of the relativistic radiation reaction force is not the one we use here. The correct formula is an open issue with no definite answer found in the literature as of today. There are various problems, such as the dependence of the force on the derivative of the acceleration and the resulting appearance of runaway solutions, and one needs to seek approximate solutions. In our case, the motion of the particles happens in the extreme relativistic limit $\Gamma \gg 1$ where eq. 3.13 in adequate but still needs to be treated carefully numerical-wise (see sec. 4.4).

Taking all the above into account, the system of differential equations to be solved is the following:

$$\left\{\begin{aligned} \frac{d\boldsymbol{u}}{dt} &= \frac{e}{m_e}\left(\boldsymbol{E} + \frac{\boldsymbol{u}}{\Gamma c} \times \boldsymbol{B}\right) - \frac{P_{rad}}{m_e \Gamma c^2}\boldsymbol{u} \\ \frac{d\boldsymbol{r}}{dt} &= \frac{\boldsymbol{u}}{\Gamma} \end{aligned}\right\} \Rightarrow$$

$$\left\{\begin{aligned} \dot{u_R} &= \frac{e}{m_e}\left(E_R + \frac{u_\phi B_z - u_z B_\phi}{\Gamma c}\right) + \frac{u_\phi^2}{\Gamma R} - \frac{P_{rad}}{m_e \Gamma c^2} u_R \\ \dot{u_\phi} &= \frac{e}{m_e}\left(\frac{-u_R B_z}{\Gamma c}\right) - \frac{u_\phi u_R}{\Gamma R} - \frac{P_{rad}}{m_e \Gamma c^2} u_\phi \\ \dot{u_z} &= \frac{e}{m_e}\left(\frac{u_R B_\phi}{\Gamma c}\right) - \frac{P_{rad}}{m_e \Gamma c^2} u_z \\ \\ \dot{R} &= \frac{u_R}{\Gamma} \\ \dot{\phi} &= \frac{u_\phi}{\Gamma R} \\ \dot{z} &= \frac{u_z}{\Gamma} \end{aligned}\right\} \tag{3.16}$$

Here, $\boldsymbol{r}$ is the position vector (R, ϕ, z) in cylindrical coordinates and we have also used the fact that $E_\phi = E_z = B_R = 0$ everywhere in our problem. The terms $\frac{u_\phi^2}{\Gamma R}$ and $\frac{u_\phi u_R}{\Gamma R}$ that appear in the first two equations are centrifugal terms that come from the differentiation in cylindrical coordinates.

In order to solve the system we need initial conditions. We assume that the particles are injected in the upper boundary of the dissipation zone , in various radial positions. The choice of the initial azimuth is arbitrary because of the axisymmetry. In total we have

$$\left\{ \begin{array}{l} z_{inj} = +h \\ R_{inj} = R_{\ell c} + w\Delta, \text{ where } 0 < \text{w} < 1 \\ \phi_{inj} = 0 \end{array} \right\}. \tag{3.17}$$

The velocity of the particles at the injection point has two components: one parallel to the magnetic field $u_{\parallel\ inj}$ because particles follow field lines from the polar cap to the DZ and a drift component $u_{d\ inj}$ which is perpendicular to the magnetic field. The latter is given by

$$\boldsymbol{u}_{d\ inj} = \Gamma c \frac{\boldsymbol{E} \times \boldsymbol{B}}{\boldsymbol{B}^2} = \Gamma c \frac{E_R B_\phi \hat{\boldsymbol{\phi}} - E_R B_\phi \hat{\boldsymbol{z}}}{B_\phi^2 + B_z^2} \tag{3.18}$$

with

$$u_{d\ inj} = \frac{E_R^2}{B_\phi^2 + B_z^2}. \tag{3.19}$$

ring of fire pulsar

The parallel component is calculated in terms of the value of the Lorentz factor at the injection point and the drift velocity as

$$\begin{aligned} & u_{\parallel\ inj}^2 + u_{d\ inj}^2 = c(\Gamma_{inj}^2 - 1) \Rightarrow \\ & u_{\parallel\ inj} = c \left[\Gamma_{inj}^2 \left(1 - \frac{E_R^2}{B_\phi^2 + B_z^2} \right) - 1 \right]^{1/2}. \end{aligned} \tag{3.20}$$

Combining these we can find the components of the initial velocity in terms of the field values and the injection Lorentz factor, which is a free parameter and depends on the energy that the particles acquired in the polar cap

$$\left\{ \begin{array}{l} u_{R\ inj} = 0 \\ u_{\phi\ inj} = \dfrac{u_{\parallel\ inj}|B_\phi| - u_{d\ inj}|B_z|}{(B_\phi^2 + B_z^2)^{1/2}} \\ u_{z\ inj} = \dfrac{-u_{\parallel\ inj}|B_z| - u_{d\ inj}|B_\phi|}{(B_\phi^2 + B_z^2)^{1/2}} \end{array} \right\} \tag{3.21}$$

In the next section we present the numerical setup we used to solve the system 3.16 with the boundary conditions 3.17 and 3.21

4 Numerical Setup

4.1 The Numerical Code

We have developed an extensive numerical code that routinely calculates relativistic particle orbits with radiation losses and the resulting high energy spectra. The code is written in the Python 3.7 programming language (`https://www.python.org/`). In particular we use the NumPy package for the calculations and data management. The differential equation system 3.16 is solved using the Odeint function of the scipy.integrate package. All the figures and plots produced by the code are handled by the Matplotlib library. In addition, a variety of secondary packages and modules were used in order to produce and process the results apart from the aforementioned three.

4.2 Nondimensionalisation

In order to handle the equation system 3.16 numerically we need to write it in a dimensionless form. We assume characteristic scales for the physical quantities that participate in the equations and then express all other values in terms of these units.

We start with the trivial selection of c as the unit for velocity so $u' = \frac{u}{c}$. Another easy and obvious choice is to measure the magnetic field in terms of its value at the LC, $B' = \frac{B}{B_{\ell c}}$. The same unit is used for the electric field as well because they are of the same order of magnitude, $E' = \frac{E}{B_{\ell c}}$. Next we consider the cyclotron frequency of an electron gyrating in the characteristic magnetic field $\omega_B = \frac{eB_{\ell c}}{m_e c}$ as the order of magnitude for time, therefore $t' = \omega_B t$. From here on the units are straightforward. Distances are measured in terms of the cyclotron Larmor radius $r_L = \frac{\Gamma m_e c^2}{eB_{\ell c}}$. Energy is measured in terms of the electron rest mass $m_e c^2$ and power has the unit $ecB_{\ell c}$.

One final detail, although it is not related to nondimensionalisation is that everywhere in the code we calculate the Lorentz factor immediately form the 4-velocity through the relationship[1]

$$u^2 = \Gamma^2 - 1 \Rightarrow \Gamma = \sqrt{u_R^2 + u_\phi^2 + u_z^2 + 1}. \tag{4.1}$$

The system becomes immediately dimensionless if we divide the first three equations of 3.16 by the factor $c\omega_B$ and the last three equations by the factor c. Every quantity in the code, either directly calculated by the integration or by post-processing, is expressed in the above units. However in all outputs we apply the transformations needed to present the results in cgs units.

[1]The only exception is in the initial conditions where we give the initial Lorentz factor Γ_{inj} and determine the initial velocities from eq. 3.21.

4.3 Parameters

We consider physical parameters relevant to the Crab pulsar:

$$
\begin{aligned}
P &= 3.34 \times 10^{-2}\ s \\
R_{\ell c} &= \frac{c}{\Omega} = 1.59 \times 10^{8}\ cm \\
B_{*} &= 3.79 \times 10^{12}\ G \\
B_{\ell c} &= \left(\frac{R_{\ell c}}{r_{*}}\right)^{3} B_{*} = 1.58 \times 10^{6}\ G
\end{aligned}
\tag{4.2}
$$

In our model we have two free parameters: the multiplicity k and the initial Lorentz factor Γ_{inj} which depends on the energy of the particles when they escape the polar cap. Crab is a young and energetic pulsar so k should be $\gg 1$ but not too high because then the magnetosphere would be almost ideal. Furthermore the particles are not mono-energetic, so the values of Γ_{inj} must follow a distribution. We arbitrarily chose a mean value and a Maxwell distribution around it because the exact type is not too important. Ideally a more careful approach or an adoption of a distribution from a polar cap model is required in a future, more detailed work. The values of the free parameters that best serve the purposes of this study are

$$
\begin{aligned}
k &= 500 \\
\langle \Gamma_{inj} \rangle &= 500
\end{aligned}
\tag{4.3}
$$

Now from eq. 3.6, 3.7, the boundaries of the DZ are

$$
\begin{aligned}
\Delta &= \frac{R_{\ell c}}{k} = 3.2 \times 10^{5}\ cm \\
h &= \frac{\langle \Gamma_{inj} \rangle mc^{2}}{eB_{\ell c}} = 6 \times 10^{-1}\ cm,\ R < R_{\ell c} + \Delta.
\end{aligned}
\tag{4.4}
$$

Out of the DZ where there is no injection of fresh particles h must be significantly smaller because the ECS is supported by particle orbits that have been flattened to the equator. We implement this effect by hand

$$
h_{ECS} = \frac{1}{10} \frac{\langle \Gamma_{inj} \rangle mc^{2}}{eB_{\ell c}} = 6 \times 10^{-2}\ cm,\ R > R_{\ell c} + \Delta. \tag{4.5}
$$

Of course in reality the decrease of the ECS height is gradual and maybe more steep than our assumption but we found that all the relevant effects on the particle trajectories and emission are still evident.

We inject both electrons and positrons coming only from the north pole in various positions. Each particle has a different initial Lorentz factor, randomly selected from a sample that follows the aforementioned Maxwell distribution. We integrate for a time interval T large enough to allow particles to travel a few times (not more because we want keep the problem local) the width of the DZ. We will explain in chapter 5 why we want to do this, but we stress here that this time interval is significantly larger than the simple estimate $T \sim \frac{c}{\Delta}$ due to the fact that the particles are deflected to the azimuthial direction by the presence of B_z.

4.4 Treatment of Radiation Losses

The problem would be very well defined and straightforward to solve if the radiation reaction force was absent. The reason why this term imposes complications for the numerical treatment is the dependence of eq. 3.13 on acceleration through eq. 3.15. The integrator (odeint) that we use to solve the system works only for first order differential equations and does not have an internal method to cope with such terms (notice that we have converted system 3.16 to six first order equations instead of three second order equations for this reason). The way that the acceleration finds its path in the radiation term makes it virtually impossible to disengage it and pass it to the left-hand side. The differential equation of each one of the spacial components of the 4-velocity depends on the total 3-acceleration in the denominator of the radiation term. Of course radiation reaction is a key element in our model so we need a different strategy to bypass this obstacle.

The course of action we chose is to calculate the radius of curvature inside the integration loop at each time step. At some time t_n we use the value of R_c from the previous time step t_{n-1}. The integrator takes the system of equations, the initial conditions and a set of time points as input and gives the values of the functions in these time points as an output. However it does not keep track of the derivative and any intermediate time points that it uses for the calculations. These values are only 'alive' during each loop of the integration and this is why we need to calculate R_c inside the loop. In order to do this we must express R_c in terms of the 4-velocity $\boldsymbol{u}$ and its derivative $\frac{d\boldsymbol{u}}{dt}$. We start from eq. 3.15 and we replace the 3-velocity so

$$R_c = \frac{\left|\frac{\boldsymbol{u}}{\Gamma}\right|^3}{\left|\frac{\boldsymbol{u}}{\Gamma} \times \frac{d}{dt}(\Gamma \boldsymbol{u})\right|} = \frac{u^3}{\Gamma^2 \left|\boldsymbol{u} \times \left(\boldsymbol{u}\frac{d\Gamma}{dt} + \Gamma\frac{d\boldsymbol{u}}{dt}\right)\right|}. \tag{4.6}$$

We calculate $\frac{d\Gamma}{dt}$ differentiating eq. 4.1

$$u\frac{du}{dt} = \Gamma\frac{d\Gamma}{dt} \Rightarrow \frac{d\Gamma}{dt} = \frac{u}{\Gamma}\frac{du}{dt} \tag{4.7}$$

Now the R_c is only a function of $\boldsymbol{u}$ and $\frac{d\boldsymbol{u}}{dt}$ and we can determine its value and therefore the radiation reaction force in every time step. The radius of curvature should change very little from one point of the orbit to the next, especially if the time resolution is high, so we expect only small errors from this trick. We performed various tests of this method to differential equations with known analytical solutions and compared the results. The verdict is that there is no important deviation from the correct solution given that the term that depends on the acceleration is sufficiently small.

4.5 Treatment of Spectral Energy Distribution

The accelerated particles follow curved gyrating trajectories and emit high-energy radiation along the instantaneous direction of their motion. The radiation spectrum emitted at every point of the orbit depends on the instantaneous Lorentz factor Γ and radius of curvature R_c. We assume for simplicity that the single particle spectrum is a δ - function around the instantaneous critical energy

$$\epsilon_{crit} = \frac{6\pi\hbar c\Gamma^3}{eR_c} \tag{4.8}$$

and the energy radiated is equal to

$$d\epsilon = dtP_{rad} = dt\frac{2e^2c\Gamma^4}{3R_c^3} \tag{4.9}$$

where $dt = t_n - t_{n-1}$.

To build the **spectral energy distribution** (SED) we need to proceed with the following steps:

- We create a binned energy space. The best choice is a logarithmic binning because the range of energies is fairly big.
- For each point of the trajectory of each particle we calculate the critical energy. If it falls in the range $\epsilon_{N+1} - \epsilon_N$ we add the energy contribution (eq. 4.9) and divide the total energy collected in each bin $\mathcal{E}_N$ by the width of the bin $\Delta\epsilon$.
- Our code is able to handle a few hundreds of particles at each run, so we need to rescale the number to match the real electron-positron flow through the DZ. At an interval dt a total number density of $2k\rho_{gj}/e$ enters the DZ - which has a total surface of $2\pi R_{\ell c}\Delta$ - at the speed of light. The rescaling is then done by multiplying $\mathcal{E}_N$ by the factor $2kB_{\ell c}\Delta c dt/e$.
- We want to have units corresponding to luminosity in the vertical axis so we need to further multiply $\mathcal{E}_N$ by the mean energy of the bin ϵ_N and divide by the time interval dt.

In the next chapter we will present particle orbits and high energy spectra that we were able to produce with our code and discuss the insight they provide us in understanding the pulsar high energy emission.

5 Results

5.1 Particle Trajectories

5.1.1 Type

The particles that enter the DZ follow **relativistic Speiser orbits** (Speiser, 1965; Uzdensky, Cerutti, and Begelman, 2011). This type of orbit occurs in recconection layers where both a reversal of the magnetic field and an accelerating electric field is present. It has some similarities with the well known synchrotron motion, but has very interesting and unique features which we will highlight below for the particular case of the 'ring of fire' model.

A particle, say a positron, enters the DZ with a velocity almost perpendicular to the equatorial plane and with $\Gamma_{inj} \gg 1$. In this region there are three dominant components of the E/M field: E_R, B_ϕ and B_z (see eq. 3.8). Each one of them has a contribution to the shape of the orbit. When the particle is injected it is forced to gyrate around B_ϕ. If the initial Larmor radius is smaller than the local thickness of the current sheet, the orbit will be completely confined inside the reconnection layer. On the other hand if $r_L > h$ the positron will get in and out of the reconnection layer. In either the particle will experience the presence of the accelerating electric field E_R. The electric field increases the energy of the particle and as a result r_L also increases. This means that the particle's orbit would get closer to the equatorial plane in each cycle. When the particle crosses the equatorial plane it is forced to gyrate in the opposite direction because of the change in the sign of B_ϕ, so it again moves towards the equatorial plane. In combination, the particle follows a meandering path which gradually shrinks towards the centre of the current sheet and stretches towards the direction of E_R (or to the opposite direction for an electron). A sketch of a Speiser orbit can be seen in fig. 5.1 (note that the coordinate system in the figure is different from the one we use in our model) . The trajectory would entirely lie in the poloidal plane if there was no B_z. However, its presence causes the overall motion of the particle to deflected in the azimuthial direction (see fig. 5.3, 5.7).

We indeed observe all these features in the orbits we calculate. Positrons and electrons follow similar orbits inside the DZ but in different directions. Things become interesting when the particles reach the ends of the DZ and enter the separatrix and equatorial current sheets. We will examine the behaviour of each type of particles separately.

5.1.2 Positrons

A typical example of the 3D trajectory of positrons calculated from our code is the one presented in fig. 5.2, 5.3. In this case we inject the positron with initial Lorentz factor $\Gamma_{inj} = 500$ at the inner boundary to see the full extent of the phenomenon. The detail on fig. 5.2 shows that, indeed, the positron moves along a Speiser orbit. A careful look at the detail reveals the stretching of the orbit. The shrinkage of the trajectory is very fast, the positron very quickly has its Larmor radius increased and approaches the equatorial plane. Notice that the scale of the vertical axis is extremely

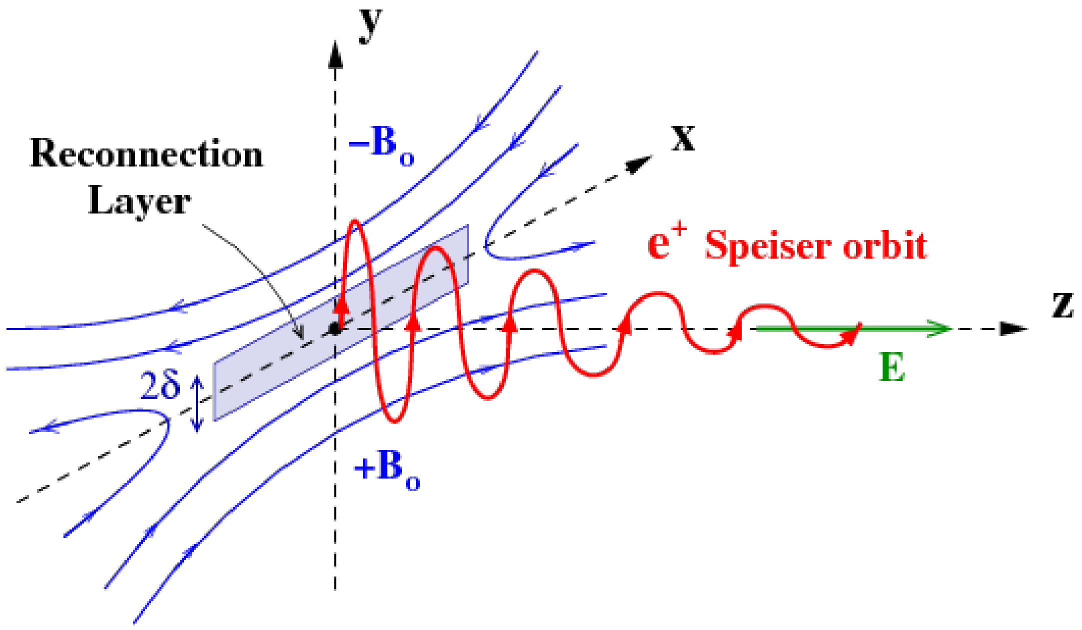

FIGURE 5.1: A sketch of a relativistic Speiser orbit, i.e., the trajectory of a charged particle (here a positron) moving back and forth across the reconnection layer of some thickness 2h. The particle is accelerated along the z-direction by the accelerating electric field, E. The initial reconnecting magnetic field is along the ±x-directions ($\pm B_{\ell c}$), and reverses across the equatorial plane (Cerutti et al., 2013).

smaller than the scale of the horizontal axis. This means that the orbit is, in reality, almost straight. When the positron reaches the end of the DZ and enters the dissipationless ECS, the stretching and shrinking stop due to the disappearance of the parallel electric field, but other than that the orbit remains the same. In fig 5.3 we see the deflection of the orbit to the azimuthial direction, following the rotation of the pulsar. Contrary to the first impression the deflection does not follow a straight line but a curved one inside the DZ. Outside of the DZ there is no deflection because there is no B_z. This is an important component of the overall motion of the positron because it produces non negligible curvature radiation. The deflection effect is also crucial for the calculation of accurate lightcurves and phase resolved spectra, albeit we did not include such calculations in our study.

To better understand the motion of the positron and to delve deeper into the radiation it produces, we show at fig. 5.4 and 5.5 the evolution of the positron's Lorentz factor and the orbit's radius of curvature with time.

The important thing to notice in fig. 5.4 is that the positron radiates a very small amount of its energy inside the DZ[1]. It takes a few more widths for the particle to radiate a significant portion (30-40%) of its kinetic energy. In a sense, high energy photons are emitted all along the ECS. We arrive, thus, at the conclusion that the dissipation zone, where the energy of the magnetic field is transformed to particle kinetic energy, does not coincide with the radiation zone, where the particle kinetic energy is transformed to high energy radiation.

[1]Given our model parameters the particle does reach or even comes close to reach the radiation reaction limit, where the radiation reaction force balances the acceleration from E_R. We calculated the evolution of Γ for a particle without radiation losses and the maximum Γ acquired inside the DZ was slightly greater than the Γ shown in fig. 5.4 because the acceleration term dominates in the equation of

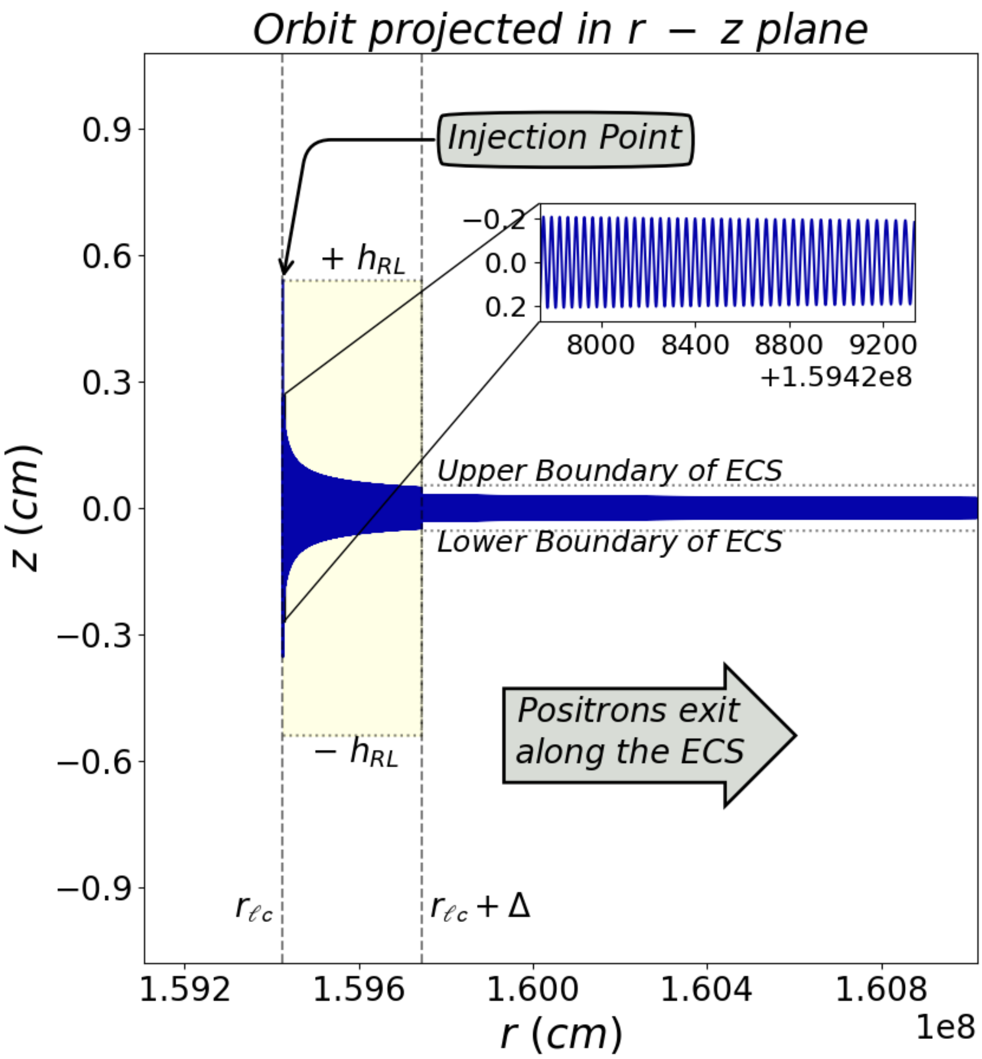

FIGURE 5.2: Projection of a 3D positron trajectory at the (r, z) plane with detail of the Speiser orbit. The positron is injected at the inner edge of the equatorial reconnection layer with $\Gamma_{\text{inj}} = 500$ (blue line). Shown also various characteristic positions of the orbit. Notice the smallness of the z-scale. The positrons are accelerated outwards by the radial electric field. After they exit the reconnection layer, they enter and support the positively charged dissipationless equatorial current-sheet (ECS) where they experience no further acceleration, and radiate away their energy.

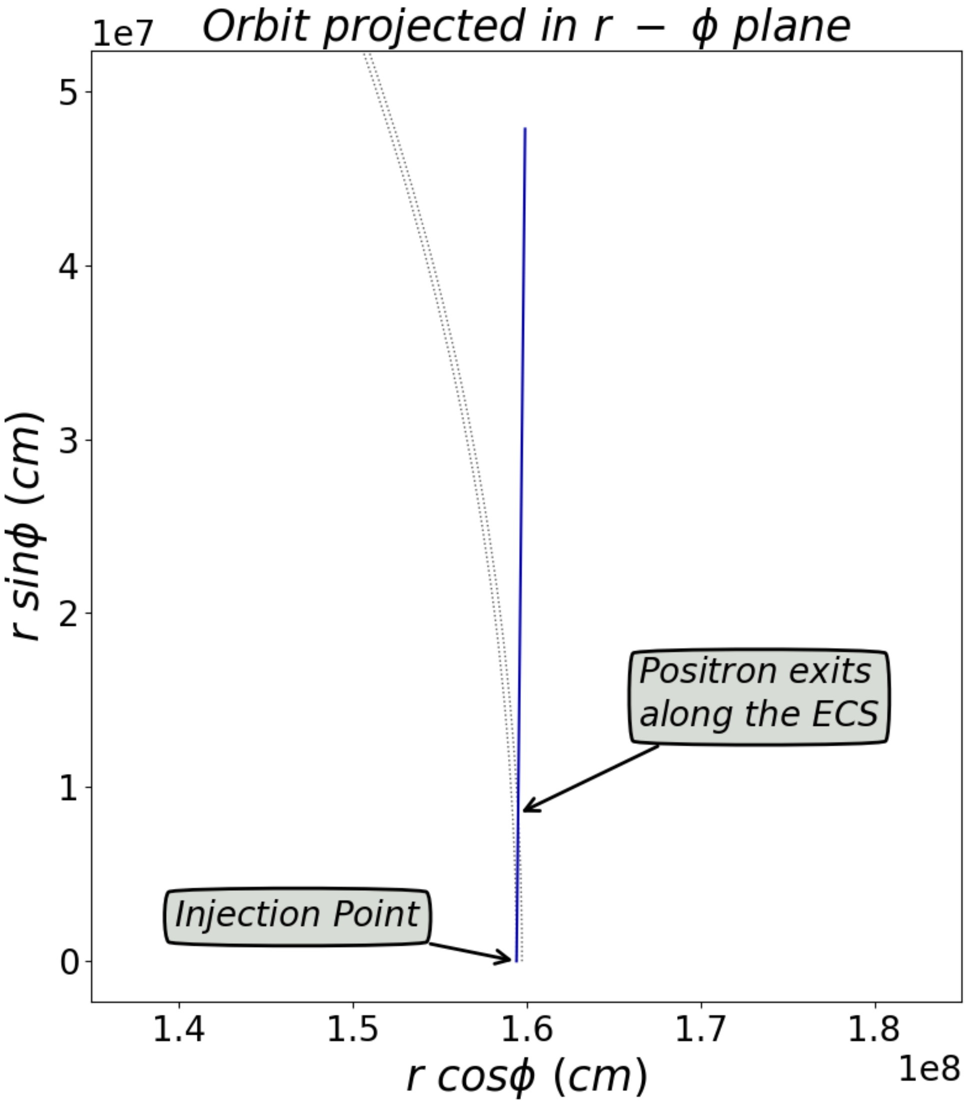

FIGURE 5.3: Projection of 3D positron trajectory in the equatorial (r, ϕ) plane (reconnection layer shown from above). The positron is injected at the inner edge of the equatorial reconnection layer with $\Gamma_{\rm inj} = 500$ (blue line). Shown also various characteristic positions of the orbit. The positrons are deflected in the ϕ direction away from the star.

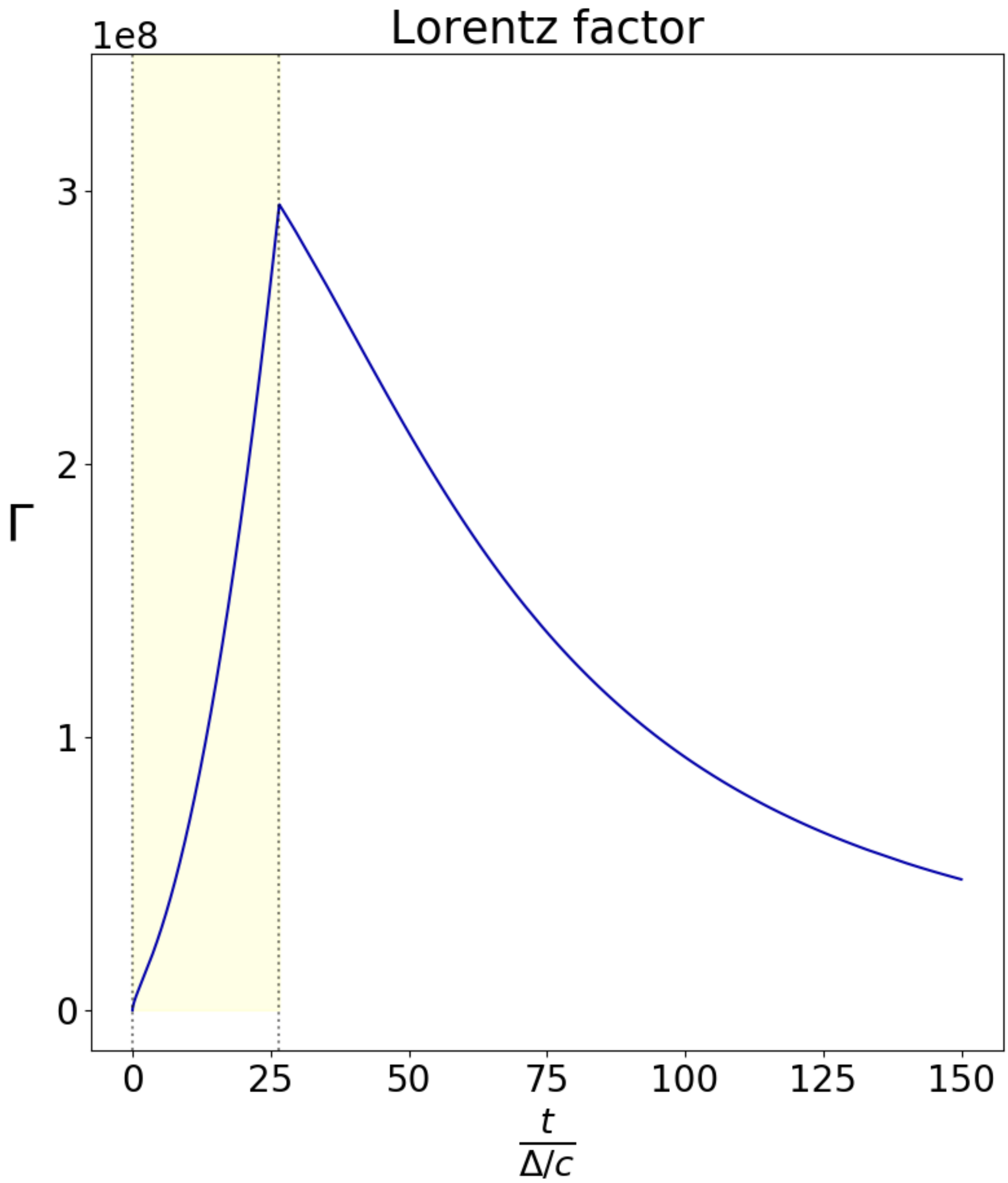

FIGURE 5.4: Evolution of the Lorentz factor Γ with time along the positron orbit. Time is in units of the dissipation layer radial light-crossing time $\frac{\Delta}{c}$. Yellow time interval: time inside the dissipation layer.

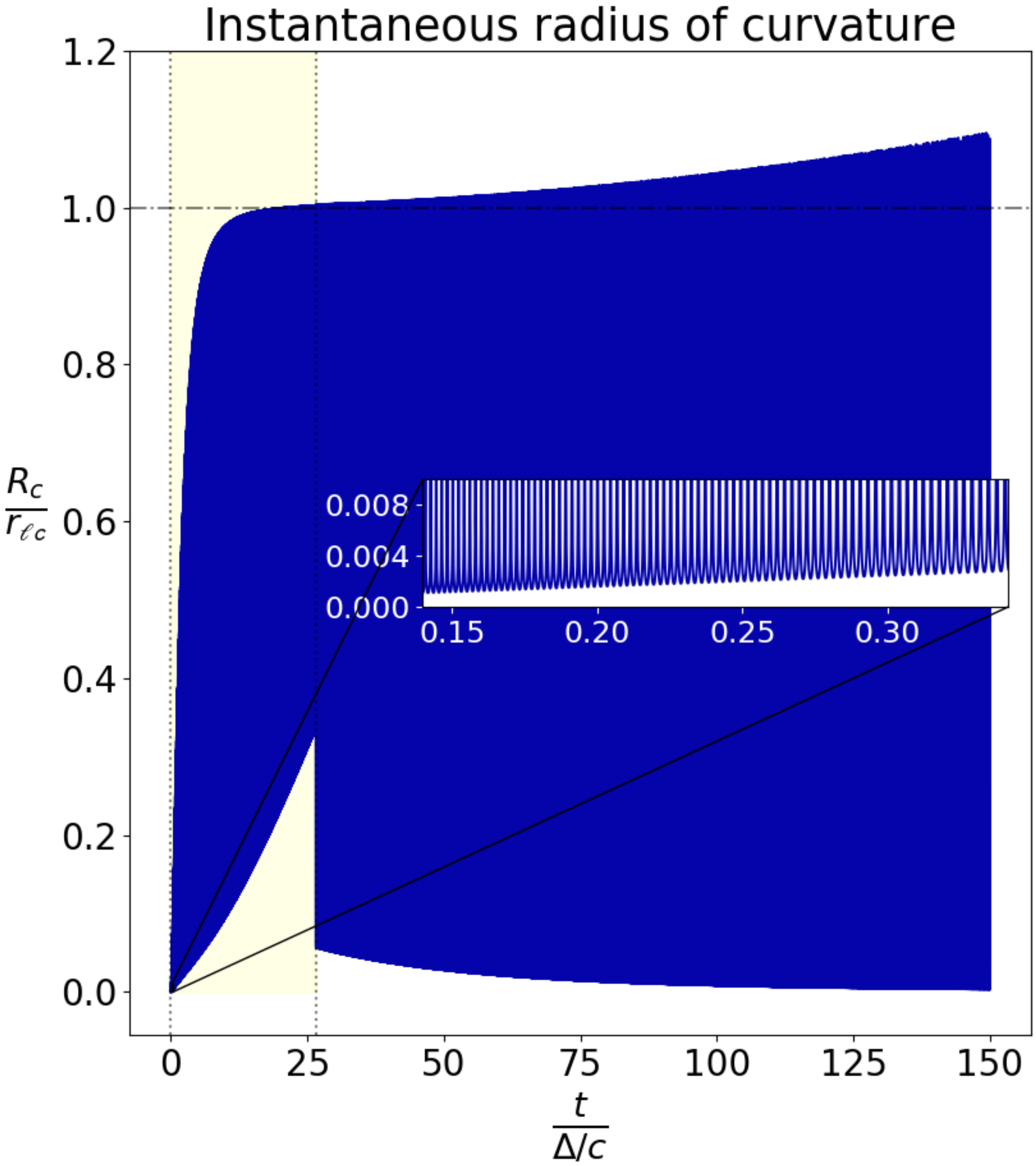

FIGURE 5.5: Evolution of the instantaneous radius of curvature R_c with time along the positron orbit. R_c is in units of $R_{\ell c}$. Time is in units of the dissipation layer radial light-crossing time $\frac{\Delta}{c}$. Yellow time interval: time inside the dissipation layer. The detail corresponds to the detail of figure 5.2.

The radius of curvature of the positron trajectory inside the DZ never surpasses $R_{\ell c}$. Its lower limit follows the deflection of the orbit. The detail of the plot reflects the sinusoidal-looking Speiser orbit. The radius of curvature reaches its lower limit every time the positron reaches the maximum height above the equatorial plane and goes to 'infinite' every time the particles crosses the equatorial plane. Once the positron gets out of the DZ there is neither an upper nor a lower limit for R_{curv} because the stretching as well as the deflection are absent. The trajectory simply adjusts to the new height $h_{ECS} = 0.1h$ and is completely dictated by B_ϕ and by the radiation losses.

5.1.3 Electrons

Following the same recipe we did for the positron, we present in fig. 5.6, 5.7 a 3D orbit for an electron. We inject it at the outer boundary of the DZ because it is accelerated inwards with $\Gamma_{inj} = 500$. As expected the orbit of the electron inside the DZ is a Speiser orbit, exactly the same as the positron. The stretching of the orbit is more intense in the case of the electron because the electric field is stronger at the injection point, $E_R = \frac{R}{R_{\ell c}} B_z$. The similarities end when the electron reaches the inner end of the DZ. At that point the electron enters a region with significantly stronger magnetic field and electric field. It is immediately forced to gyrate around B_z and move along it, getting in and out of the DZ. The electron, thus, leaves the equatorial plane and supports the SCS. This is a motion with different characteristics in relation to the motion of the positron so it produces a different emission pattern. We will explain more on this in the next section. As far as the azimuthial deflection is concerned, it is smoother than the deflection of the positron and to the opposite direction. The electron ends up sticking at the inner boundary of the DZ where it follows the magnetic field all the way back to the star.

In fig. 5.8 and 5.9 we clearly see the effects of the second part of trajectory. Inside the dissipation zone the electron Lorentz factor increases much like the positron. Notice the difference in the curvature of the line which is caused by the fact that the electron moves along a decreasing E_R while the positron moves along an increasing E_R. When the electron leaves the DZ it successively enters the closed line region with E_R much greater than that of the DZ where $E_R = \frac{R}{R_{\ell c}} B_z$. This is because E_R is directly proportional to B_z. This results in the formation of the tips in the line $\Gamma(t)$. Simultaneously the particle loses energy due to radiation so Γ decreases with time. Correspondingly the evolution of the instantaneous radius of curvature with time outside of the DZ shows the increased scale of the orbit due to increased magnetic field.

5.2 High-Energy Spectra

All the particles, regardless of their injection position and the initial Lorentz factor, follow the trajectories described in the above sections. The only features that depend on the initial conditions are the amount of energy that the particle acquires inside the DZ and whether the orbit lies entirely between the upper and lower limit of the DZ and the ECS. Both of these features affect the emission we receive from the particle, particularly the second. A particle that spends most of its travel time out of the region where the reversal of the magnetic field takes place (or equivalently their

motion. This means that the total power radiated inside the DZ is negligible compared to the power radiated in the ECS.

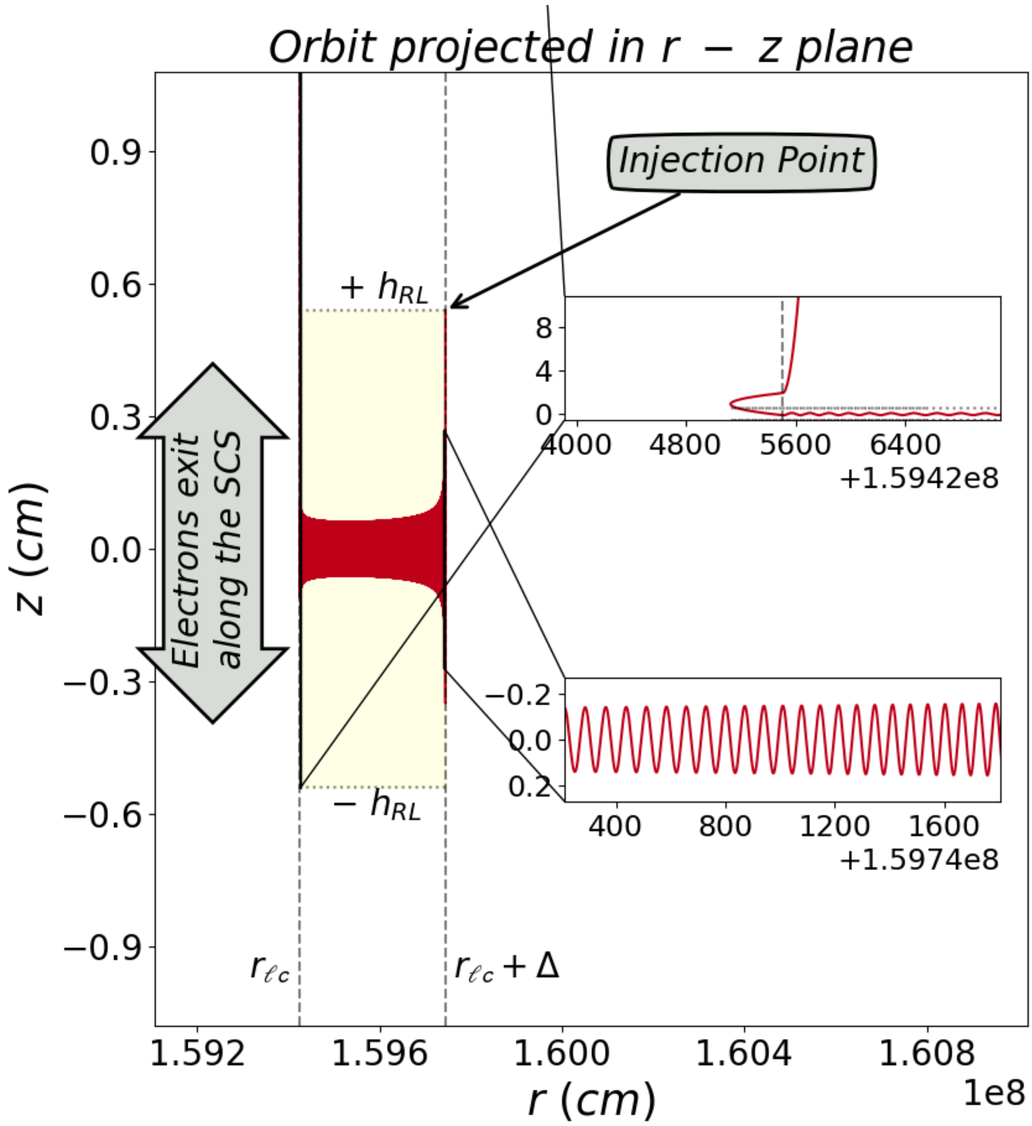

FIGURE 5.6: Projection of a 3D electron trajectory at the (r, z) plane with detail of the Speiser orbit. The electron is injected at the outer edge of the equatorial reconnection layer with $\Gamma_{\rm inj} = 500$ (red line). Shown also various characteristic positions of the orbit. Notice the smallness of the z-scale. The electrons are accelerated inwards by the radial electric field. After they exit the reconnection layer, they enter and support the negatively charged dissipationless separatrix current-sheet (SCS) where they follow the magnetic field back to the star, and radiate away their energy.

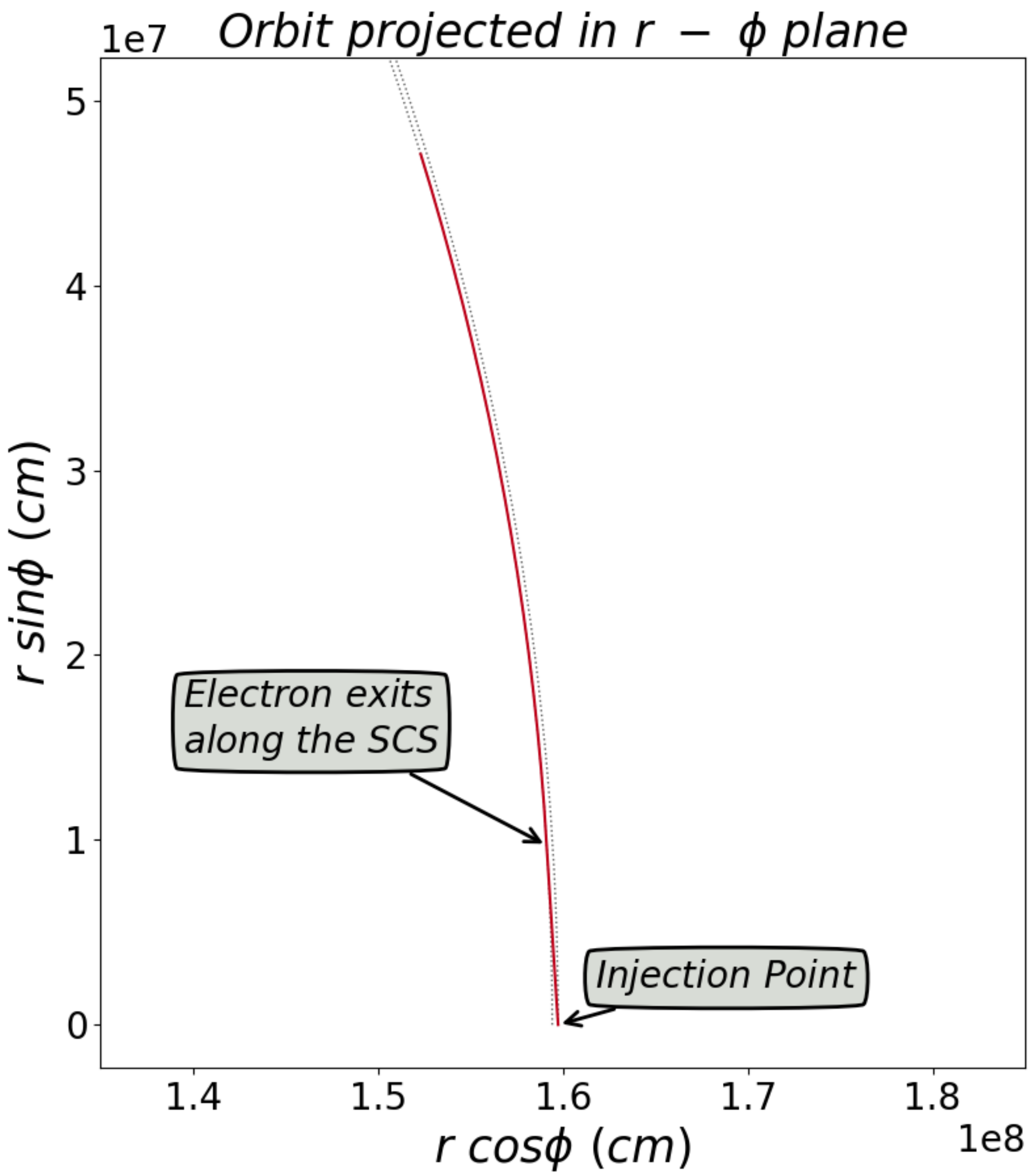

FIGURE 5.7: Projection of 3D electron trajectory in the equatorial (r, ϕ) plane (reconnection layer shown from above). The electron is injected at the outer edge of the equatorial reconnection layer with $\Gamma_{\rm inj} = 500$ (red line). Shown also various characteristic positions of the orbit. The electrons are deflected in the ϕ direction towards the star.

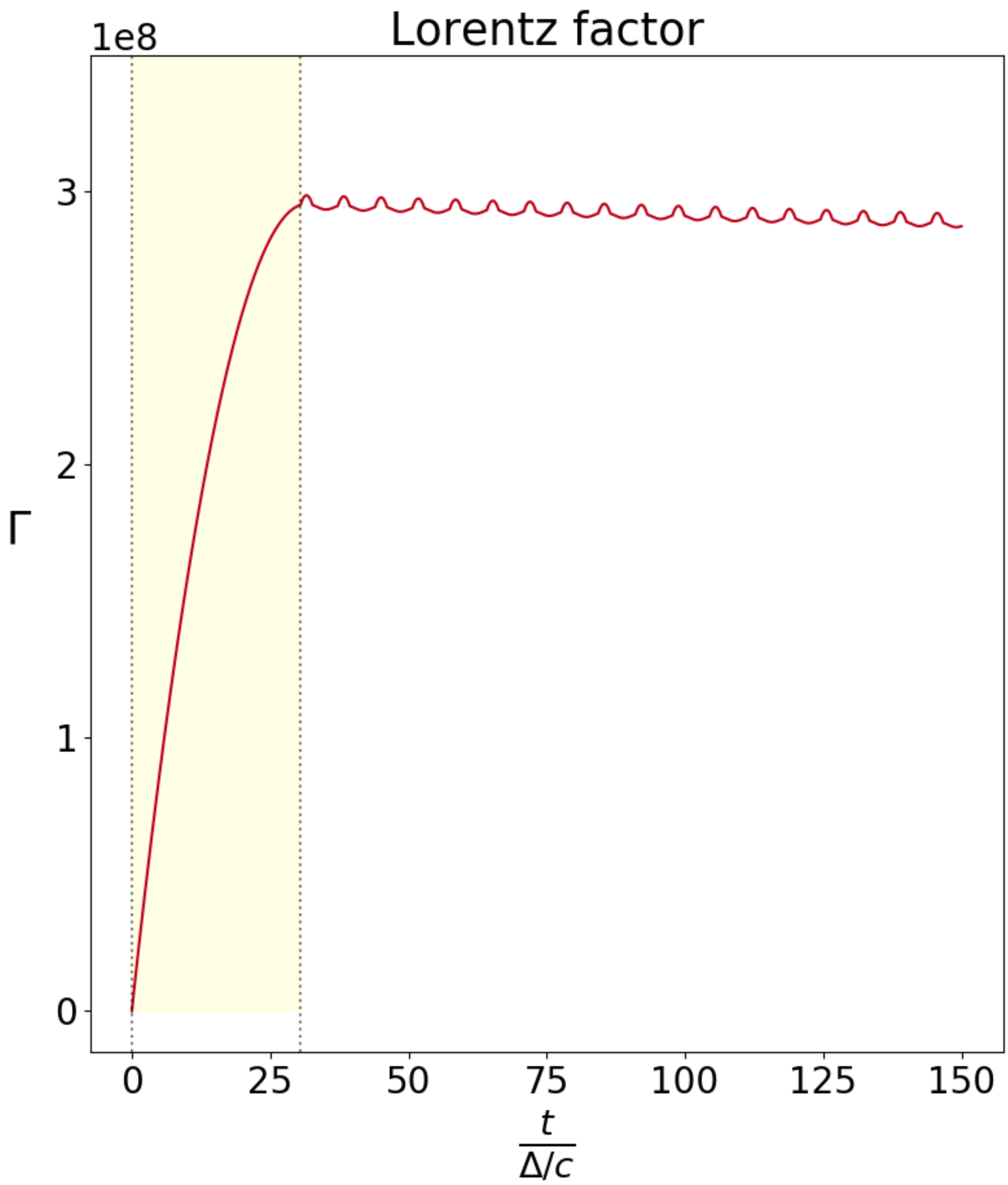

FIGURE 5.8: Evolution of the Lorentz factor Γ with time along the electron orbit. Time is in units of the dissipation layer radial light-crossing time $\frac{\Delta}{c}$. Yellow time interval: time inside the dissipation layer.

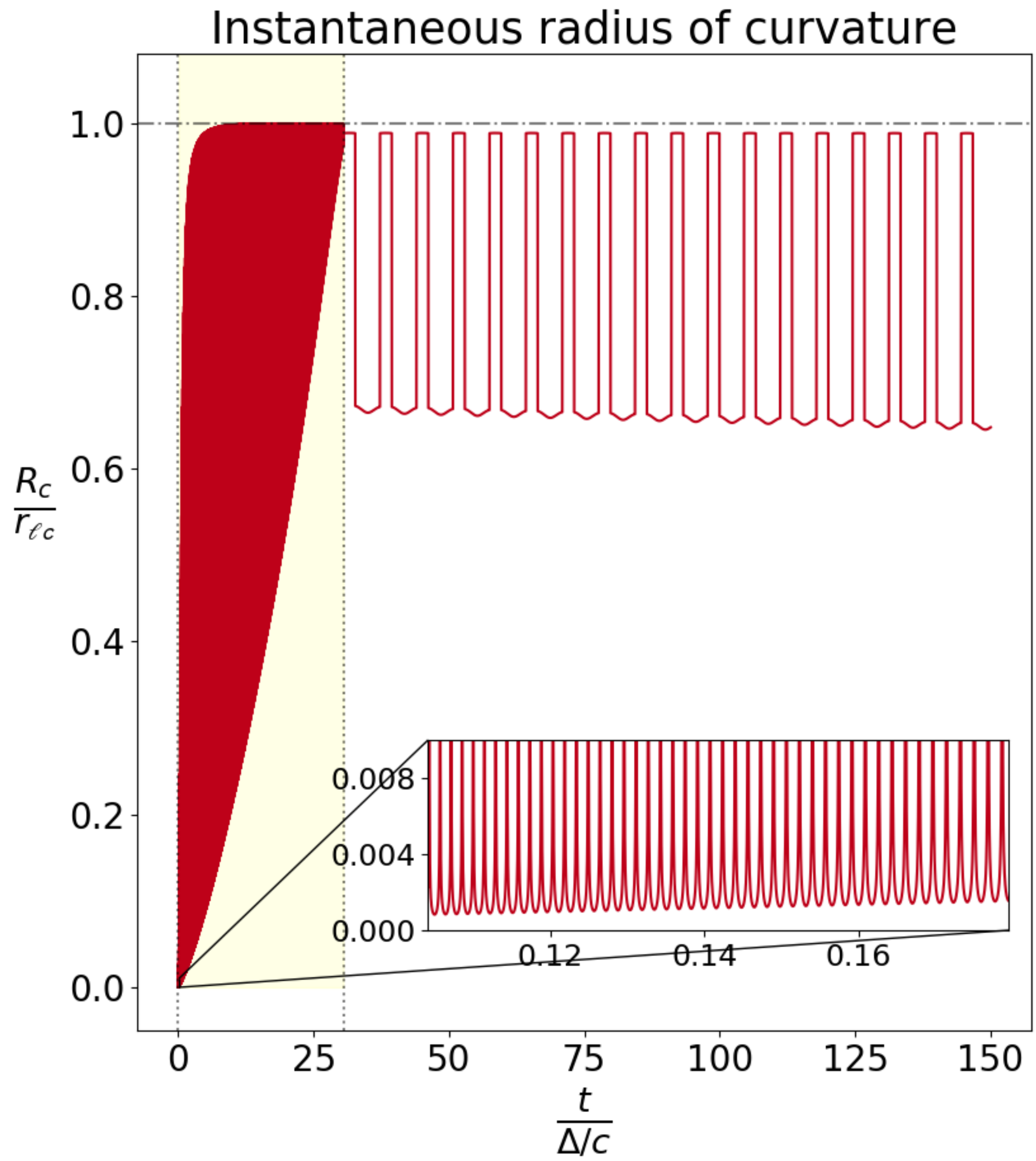

FIGURE 5.9: Evolution of the instantaneous radius of curvature R_c with time along the electron orbit. R_c is in units of $R_{\ell c}$. Time is in units of the dissipation layer radial light-crossing time $\frac{\Delta}{c}$. Yellow time interval: time inside the dissipation layer. The detail corresponds to the detail of figure 5.6.

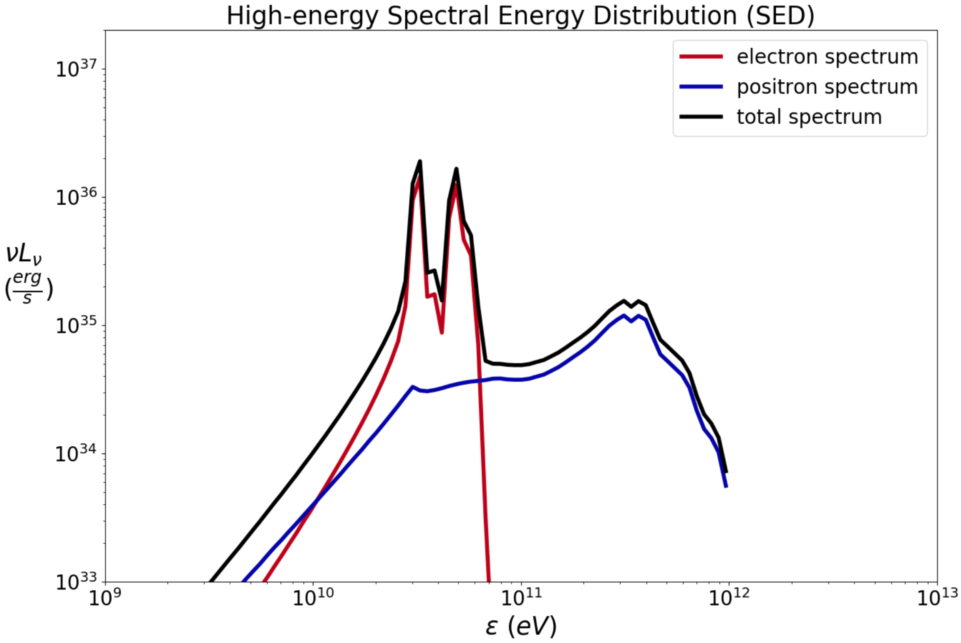

FIGURE 5.10: Calculated high-energy Spectral Energy Distribution (SED) νL_ν in $\frac{erg}{s}$. Blue line: positron contribution. Red line: electron contribution. Black line: total SED. The very high energy component that extends to the TeV range is due to the positrons that radiate away most of their energy along the equatorial current sheet. The electrons must travel a large distance along the separatrix return current sheet before they radiate away most of their energy, possibly in a different part of the spectrum.

Larmor radius is greater than h) suffers from strong losses because it deals with an intense magnetic field. On the contrary a particle whose orbit is flattened and confined in the equatorial plane travels in a region with almost negligible magnetic field and therefore the radiation losses are small. For this reason it is important to inject particles with a variety of Γ_{inj} which is the parameter that determines the height of the orbit.

On the other hand, the radial position at which the particles are injected regulates the total amount of energy that is transported to them from the electromagnetic field. Particles that enter at the radial boundaries of the DZ and travel its full length take advantage of all the potential drop and gain all the available energy. It is not too problematic to assume that the greatest contribution to the high energy spectrum comes from the population of positrons and electrons that enter the DZ from the inner and outer boundaries, respectively. There is no need to spent computational effort in calculation particles that enter the DZ in intermediate positions. This way we are able to calculate orbits with a more diverse sample of Γ_{inj}. Indeed our calculations show that the main characteristics of the spectrum depend on these populations and are weakly affected from the rest of the particles.

In fig. 5.10 we show the SED that our code produced by integrating ~ 100 orbits, following the steps of sec. 4.5 and taking under consideration the above arguments. We see that each particle species contributes to the spectrum in a different way, an expected result due to their behaviour outside of the DZ.

We acknowledge that there are some important limitations of our analysis. Firstly, we are not allowed to integrate particle orbits very far from the ring-of-fire where the electric and magnetic fields begin to diverge from the simple expressions of eqs. 3.8, 3.9, 3.10. More precisely, within the calculated part of their trajectory, the outward moving positrons managed to radiate away the largest part of the energy they gained in the DZ, and their contribution to the high-energy SED is shown in fig. 5.10. On the contrary, within the same integration time, the electrons radiated away only a very small fraction of their energy. This suggests that they will need to travel a large distance along the separatrix return current sheet before they radiate away most of their energy. The conditions in the SCS are very different from those in the ECS, and therefore, the electron contribution to the high-energy SED is expected to be very different from that of the positrons (it may, for example,account for the part of the SED that peaks around a few hundred keV). Secondly we completely ignore the geometry and the direction of emission. Instead we choose to count every photon emitted by each particle and add them to build the SED. These limitations prevent us from obtaining an SED comparable with the observations and only allow us to get an insightful qualitative picture.

.

6 Conclusions

6.1 Summary

In this thesis we proposed and investigated the 'Ring of Fire' model for the particle acceleration and high energy emission in the pulsar's magnetosphere. The key points of this model are its simplicity, its reliance on analytical assumptions to ease the numerical calculations and its ability to explain both the high energy emission and the global distribution of the charge and current density in the magnetosphere, simultaneously. The core element of the model is the development of a non-ideal narrow dissipation zone near the LC where particle acceleration takes place. Its width Δ depends on the pair production efficiency of the pulsar through the pair multiplicity k, a basic parameter in our model. We were able to calculate realistic particle orbits and illustrate them in their actual orders of magnitude without the need of scaling prescriptions. This gave us a direct insight into the conditions near the Y-point and the LC. It helped us understand the nature of the motion of the particles and the way they are redistributed into the magnetosphere. From the particle orbits we were able to obtain high energy spectra which qualitatively resemble the observations. Our results show that positrons and electrons contribute differently in the total spectrum. Despite the simplifications and the limitations we were able to reproduce, with acceptable accuracy, the maximum Lorentz factors and γ-ray energies that can be attained (10^8 and 1 TeV respectively), which encourages us to stay in this path, implementing the necessary improvements.

6.2 Discussion

In this work, our main purpose was to test simple ideas which will help us understand the behaviour of the particles and the conditions under which the high energy emission is produced. We pinpointed the various limitations of our model and gathered important knowledge to attempt to bypass them. In order to produce a more accurate, detailed, phase resolved SED we need to take into account features such as a 3D inclined pulsar magnetosphere, global distribution of E/M field, photon travel time, self consistent calculation of the DZ height h, etc. Despite these setbacks, our analysis shows that the idea of a narrow dissipation zone being the origin of particle acceleration is valid. On the other hand, during this process we managed to highlight the fundamental aspects of dissipation in the magnetosphere and acquired the technical know-how for calculating relativistic particle orbits which can be put in use in future, more sophisticated simulations.

6.3 Future Steps

The model presented in this thesis draws the basic picture of a realistic magnetosphere. The next step is to reduce the number of parameters that were imported to the model 'by hand' such as h and Γ_{inj}. This can be done either by self consistently calculating them by some iteration method or by adopting them from some other successful model. This will fix some of the inaccuracies of our model and clear the way for global solution. In the same spirit a refinement of the theoretical assumptions for the E/M field and the charge and current densities will assist in reducing the computational needs. These are modifications that apply directly to our model and improve it

The ultimate target, which our analysis attempts to lead the way to, is the development of a hybrid ideal FFE-PIC numerical code. It was argued in sec. 3.1 that the region of interest is where the acceleration and the emission takes place. This is what we study here semi-analytically and what we hope can be studied self-consistently. A numerical method that uses PIC to calculate what happens in the current sheets and then sets them as boundary conditions for a global ideal MHD simulation can successfully channel all the available computational resources where they are needed and create very accurate, high resolution results.

Bibliography

Baade, W. and F. Zwicky (1934a). “Cosmic Rays from Super-novae”. In: *Proceedings of the National Academy of Science* 20, pp. 259–263. DOI: 10.1073/pnas.20.5.259.

— (1934b). “On Super-novae”. In: *Proceedings of the National Academy of Science* 20, pp. 254–259. DOI: 10.1073/pnas.20.5.254.

Bühler, R. and R. Blandford (2014). “The surprising Crab pulsar and its nebula: a review”. In: *Reports on Progress in Physics* 77.6, 066901, p. 066901. DOI: 10.1088/0034-4885/77/6/066901. arXiv: 1309.7046 [astro-ph.HE].

Cerutti, B. et al. (2013). “Simulations of Particle Acceleration beyond the Classical Synchrotron Burnoff Limit in Magnetic Reconnection: An Explanation of the Crab Flares”. In: 770.2, 147, p. 147. DOI: 10.1088/0004-637X/770/2/147. arXiv: 1302.6247 [astro-ph.HE].

Cerutti, Benoît and Andrei M. Beloborodov (2017). “Electrodynamics of Pulsar Magnetospheres”. In: 207.1-4, pp. 111–136. DOI: 10.1007/s11214-016-0315-7. arXiv: 1611.04331 [astro-ph.HE].

Chadwick, J. (1932). “Possible Existence of a Neutron”. In: 129, p. 312. DOI: 10.1038/129312a0.

Contopoulos, I. (2019). “Current closure in the pulsar magnetosphere”. In: 482.1, pp. L50–L54. DOI: 10.1093/mnrasl/sly183. arXiv: 1809.09064 [astro-ph.HE].

Contopoulos, Ioannis, Demosthenes Kazanas, and Christian Fendt (1999). “The Axisymmetric Pulsar Magnetosphere”. In: *The Astrophysical Journal* 511.1, pp. 351–358. DOI: 10.1086/306652. URL: https://doi.org/10.1086%2F306652.

Contopoulos, Ioannis and Petros Stefanou (2019). “A ring-of-fire in the pulsar magnetosphere”. In: *arXiv e-prints*, arXiv:1903.08501, arXiv:1903.08501. arXiv: 1903.08501 [astro-ph.HE].

E, ALIU et al. (2008). “Observation of Pulsed gamma-Rays Above 25 GeV from the Crab Pulsar with MAGIC”. In: *SCIENCE* 322, pp. 1221–1224.

Espinoza, C. M. (2013). “The spin evolution of young pulsars”. In: *Neutron Stars and Pulsars: Challenges and Opportunities after 80 years*. Ed. by J. van Leeuwen. Vol. 291. IAU Symposium, pp. 195–198. DOI: 10.1017/S1743921312023629. arXiv: 1211.5276 [astro-ph.HE].

Gold, T. (1968). “Rotating Neutron Stars as the Origin of the Pulsating Radio Sources”. In: 218, pp. 731–732. DOI: 10.1038/218731a0.

Goldreich, P. and W. H. Julian (1969). “Pulsar Electrodynamics”. In: 157, p. 869. DOI: 10.1086/150119.

Harding, Alice K. (2013). “The neutron star zoo”. In: *Frontiers of Physics* 8, pp. 679–692. DOI: 10.1007/s11467-013-0285-0. arXiv: 1302.0869 [astro-ph.HE].

Hewish, A. et al. (1968). “Observation of a Rapidly Pulsating Radio Source”. In: 217, pp. 709–713. DOI: 10.1038/217709a0.

Kiziltan, Bülent et al. (2013). “THE NEUTRON STAR MASS DISTRIBUTION”. In: *The Astrophysical Journal* 778.1, p. 66. DOI: 10.1088/0004-637x/778/1/66. URL: https://doi.org/10.1088%2F0004-637x%2F778%2F1%2F66.

Michel, F. C. (1973). “Rotating Magnetospheres: an Exact 3-D Solution”. In: 180, p. L133. DOI: 10.1086/181169.

Nandi, Rana and Debades Bandyopadhyay (2012). "Magnetised Neutron Star Crusts and Torsional Shear Modes of Magnetars". In: *Journal of Physics Conference Series* 420. DOI: 10.1088/1742-6596/420/1/012144.

Oppenheimer, J. R. and G. M. Volkoff (1939). "On Massive Neutron Cores". In: *Physical Review* 55, pp. 374–381. DOI: 10.1103/PhysRev.55.374.

Pacini, F. (1967). "Energy Emission from a Neutron Star". In: 216, pp. 567–568. DOI: 10.1038/216567a0.

Scharlemann, E. T. and R. V. Wagoner (1973). "Aligned Rotating Magnetospheres. General Analysis". In: 182, pp. 951–960. DOI: 10.1086/152195.

Speiser, T. W. (1965). "Particle Trajectories in Model Current Sheets, 1, Analytical Solutions". In: 70, pp. 4219–4226. DOI: 10.1029/JZ070i017p04219.

Timokhin, A. N. and A. K. Harding (2015). "On the Polar Cap Cascade Pair Multiplicity of Young Pulsars". In: 810.2, 144, p. 144. DOI: 10.1088/0004-637X/810/2/144. arXiv: 1504.02194 [astro-ph.HE].

Uzdensky, Dmitri A., Benoît Cerutti, and Mitchell C. Begelman (2011). "Reconnection-powered Linear Accelerator and Gamma-Ray Flares in the Crab Nebula". In: 737.2, L40, p. L40. DOI: 10.1088/2041-8205/737/2/L40. arXiv: 1105.0942 [astro-ph.HE].